Application of CFD/CSD Coupling for Analysis of Rotorcraft Airloads and Blade Loads in Maneuvering Flight

Mahendra J. Bhagwat
ELORET Corp.
Ames Research Center
Moffett Field, CA 94035

Robert A. Ormiston
US Army AMRDEC
Aeroflightdynamics Directorate
Moffett Field, CA 94035

Hossein A. Saberi and Hong Xin
Advanced Rotorcraft Technology, Inc.
1330 Charleston Road
Mountain View, CA 94043

This paper presents calculations of both the rotor airloads and structural loads in the UTTAS pull-up maneuver performed under the NASA/Army UH-60A Airloads Program. These calculations were performed using a computational fluid dynamics code, OVERFLOW-2, coupled to a rotorcraft comprehensive analysis, RCAS. For the time-varying maneuver calculations, the two codes were tightly coupled, and exchanged airloads and blade structural deflections at each time step. The coupled solution methodology gives substantial improvement in airloads prediction because of the ability to model three-dimensional transonic effects on the advancing blades, stall events on the retreating blade as well as the inter-dependent blade elastic deformations. Correlation with data for both the airloads and blade structural loads is very good. The use of quasi-steady, loosely coupled solutions to model parts of the maneuver is also examined. It is found that the airloads and structural loads predictions using this approach are almost as good as those with a time-accurate tightly coupled calculation.

Introduction

One of the most important and, at the same time, difficult challenges for rotorcraft aeromechanics analysis is the accurate prediction of airloads and structural loads in maneuvering flight. Important, because some of the largest structural loads — and those that impact rotorcraft design — are usually encountered in maneuvering flight, and difficult, because of the wide range of complex aeromechanics phenomena present. Typically, rotor blade airfoils operate close to the stall region, large blade elastic deflections intensify aeroelastic phenomena and the operating environment is highly unsteady, and non-periodic. These difficulties have for many years limited the accuracy of aeromechanics analysis for high load-factor maneuvers.

One of the principal issues is the limitation of traditional rotorcraft aerodynamics methods, based on lifting line theory and various empirical models for blade unsteady airloads. A significant step in overcoming these limitations is available from computational fluid dynamics (CFD) methods. In the last several years, major advances have been made in aeroelastic coupling between CFD codes and rotor comprehensive analysis codes, encompassing relatively sophisticated rotor blade computational structural dynamics (CSD) models, and thus combine the capabilities of the individual disciplines. Most of the work has focused on the trim flight condition where the rotor operates in a steady-state periodic condition, e.g., Refs. 1–4. The periodic steady state enables simplifications of the solution procedure and also reduces computation time. For the commonly accepted CFD/CSD loose coupling procedure, CFD airloads and CSD motions are exchanged only at every trim iteration step enabling the two analyses to be performed partially independently affording certain computational advantages.

For general time dependent maneuver conditions, the CFD airloads and CSD motions need to be exchanged at every time step with a tight coupling approach. Such an approach has been employed by a number of investigators, perhaps most recently and successfully by Nygaard *et al.* (Ref. 5) and was demonstrated using simple idealized maneuvers involving transient control inputs and motions of the rotor blades but for a fixed hub without arbitrary motion of the rotor. The present work is an extension of Ref. 5. If the maneuver duration extends over many rotor revolutions, the computation time may be considerable. Therefore, the possibility of adapting the loose coupling approach for quasi-steady maneuver analyses is also explored in the present work.

The NASA-Army UH-60A Airloads Program explored a broad range of test conditions. The extensive detailed blade aerodynamic and structural loads measurements provides excellent opportunities to investigate the capabilities of new computational methods for predicting rotorcraft aeromechanics. This flight test program has been extensively documented in the literature by Bousman and Kufeld, e.g., Refs. 6–8. The envelope of test points depicted on a map of vehicle weight coefficient versus advance ratio is shown in Fig. 1. The steady state flight conditions are depicted by single points, corresponding to

Presented at the AHS 63rd Annual Forum, Virginia Beach, VA, May 1–3, 2007.

steady level flight speed sweeps at various altitudes. The upper bound of these test points defines the maximum thrust limit of the rotor due to retreating blade stall and the airfoil maximum lift coefficient. Figure 1 includes a representative maximum thrust boundary as determined by the wind tunnel tests of McHugh *et al.* (Ref. 9). The UH-60A flight test results are consistent with wind tunnel test boundary although the weight coefficient does not distinguish between the isolated rotor thrust and the fuselage, empennage, and tail rotor forces.

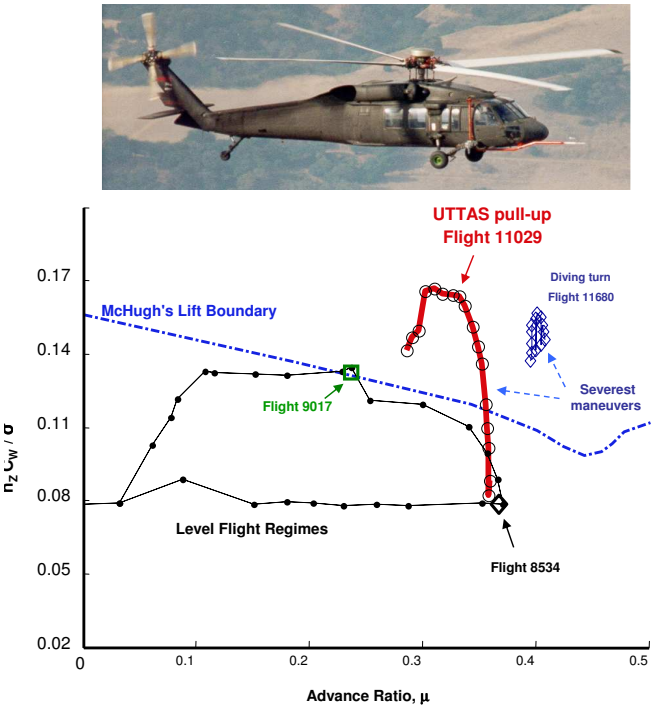

Fig. 1. UH-60A airloads program test envelope

Also included in Fig. 1 are the time varying C_W/σ vs. μ values for the UTTAS pull-up maneuver. The maneuver begins near the maximum level flight speed of the aircraft and achieves a significant normal load factor ($2.1g$) that significantly exceeds the steady state McHugh boundary ($n_Z C_W/\sigma$=0.165 vs. 0.12). It is pertinent to inquire about the mechanism responsible for this capability; this will be addressed in the paper.

Two other flight test points are of interest for the present investigation. The high speed level flight condition (counter 8534) is relevant since it closely duplicates the initial level flight conditions preceding the UTTAS pull-up maneuver. The second test point of interest is a high thrust coefficient condition at moderate flight speed lying on the McHugh boundary (counter 9017) that involves considerable blade stall. Both these test points have been extensively studied using conventional as well as CFD/CSD methods (Refs. 3, 4).

The purpose of this paper is to apply the CFD/CSD tight coupling procedure to the problem of a rotorcraft in maneuvering flight with arbitrary motion. The UH-60A UTTAS pull-up maneuver will be used for this purpose. The analytical results will be obtained using the OVERFLOW-2 CFD code coupled with the RCAS comprehensive rotorcraft analysis code. RCAS results will also be presented using conventional aerodynamics modeling for comparative purposes and to illustrate the differences between the two approaches. The present work has been conducted at the US Army Aeroflightdynamics Directorate with sponsorship of the DoD HPC Modernization Office as part of the CHSSI CST-05 Project.

The RCAS Code

The Rotorcraft Comprehensive Analysis System (RCAS) is a comprehensive multi-disciplinary, computer software system for predicting rotorcraft aerodynamics, performance, stability and control, aeroelastic stability, loads, and vibration. RCAS was developed by the Aeroflightdynamics Directorate, US Army Aviation and Missile Research, Development, and Engineering Center (RDECOM), to provide state-of-the art rotorcraft modeling and analysis technology for government, industry, and academia. The Rotorcraft Comprehensive Analysis System is capable of modeling a wide range of complex rotorcraft configurations operating in hover, forward flight, and in maneuvering conditions. The RCAS structural model employs a hierarchical, finite element, multibody dynamics formulation for coupled rotor-body systems. It includes a library of primitive elements to build arbitrarily complex models including nonlinear beams, rigid body mass, rigid bar, spring, damper, and mechanical applied load as well as hinges and slides. Rotor and fuselage modeling is fully integrated with engines, drivetrain, control systems, and aerodynamics. RCAS includes multiple aerodynamic options for airloads, wake induced flowfields, and component aerodynamic interference. Airloads models include 2-D airfoil and lifting line models for rotor blade, wings, or empennages and 3-D airloads for bodies. An overview of RCAS with selected illustrative examples and validation results is presented by Saberi *et al.* (Ref. 10). RCAS has also been used extensively and validated for other UH-60A airloads calculations (Refs. 11, 12).

RCAS UH-60A model

The UH-60A model includes a rotor and a fuselage subsystem. The vehicle reference frame, called the G-frame, is attached to the fuselage subsystem node located near the fuselage center of mass. The rotor subsystem axis is rotated forward 3 deg. with respect to the fuselage reference line. The rotor subsystem consists of four identical blades, pitch control systems, and lead-lag dampers. A finite element structural model of the UH-60A rotor blade is used for the present study. Details the blade root hinges, pitch control, and the lead-lag damper are

shown in Fig. 2. The outboard tip of the blade is swept and the structural and aerodynamic axes of the blade are twisted non-uniformly along the radius. Rigid bars and spring elements are used to represent the pitch control linkage and a slide element inputs blade collective and cyclic pitch control inputs. The spherical elastomeric bearing is represented by three coincident hinge elements for flap, lag, and pitch rotation of the blade together with accompanying values for bearing stiffness and damping for each hinge axis. Two alternative models are used for the blade lead-lag damper: a linear damper element and a simple nonlinear damper model with load saturation. A mechanical applied load element is used to apply arbitrary, time dependent forces and moments to the structure, and is used to apply the CFD airloads to the CSD model for coupled RCAS/OVERFLOW-2 analyses. Further details of the rotor blade model are found in Ref. 11

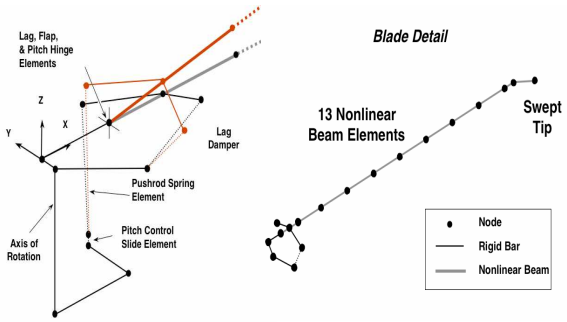

Fig. 2. RCAS finite element model for the UH-60A showing hub and blade details

Conventional aerodynamic models are used to generate baseline RCAS results for comparison with the RCAS/OVERFLOW-2. The rotor wake used simple uniform inflow momentum theory for maneuver analyses and a prescribed vortex wake model for quasi steady calculations. Airfoil tables for the two different UH-60A airfoils were used for blade airloads; both Theodorsen theory and the Leishman-Beddoes vortex shedding dynamic stall model were used for unsteady aerodynamics. The blade was modeled with 27 discrete aerosegments distributed from root to tip to represent the local spanwise twist, chord, and tip sweep of the blade planform.

The OVERFLOW-2 Code

The CFD calculations use the Reynolds-averaged Navier-Stokes CFD code OVERFLOW-2 (Refs. 13, 14). The code has been continually developed by NASA and the Army and has been applied to an ever-increasing range of fluid dynamics problems. OVERFLOW-2 incorporates modeling of time-dependent rigid-body motion of components originally developed in OVERFLOW-D, an off-shoot from a prior version of OVERFLOW-1. Additions includes, in particular, the individual rotor blade motions essential to rotorcraft calculations and the extensions to include blade elastic deformations. The coupled CFD/CSD calculations using OVERFLOW-D were reported by Potsdam *et al.* (Ref. 2), while calculations with OVERFLOW-2 and RCAS were reported by Nygaard *et al.* (Ref. 5).

OVERFLOW-2 solutions are computed on structured, overset grids. The near-body grids are body-conforming while the off-body grids are Cartesian and automatically generated (Ref. 15). Near-body grids are used to discretize the surface geometries and capture wall-bounded viscous effects. Off-body grids are clustered in several levels and extend to the far field with decreasing grid density and capture the wakes. In addition to rigid-body movement of the rotor blades due to rotor rotation, collective, cyclic, and elastic motion is introduced by the structural mechanics and dynamics. Solutions are computed on a large cluster of computers communicating with the message passing interface (MPI) protocol. Both the domain connectivity and flow solver modules have been parallelized for efficient, scalable computations using MPI.

OVERFLOW-2 UH-60A grids

The OVERFLOW-2 grids used in the present study are the grids first used by Potsdam *et al.* (Ref. 2). The coarse grid, with 4.4 million grid points, was chosen for most of the computations in the interest of computational speed. This coarse grid was shown to give very little differences in computed forces for steady level flight computations as compared to a baseline fine grid with 26.1 million grid points. Computations for one maneuver revolution are performed in the present study using both the coarse and the fine grid to verify small grid sensitivity.

A 4^{th}-order spatial central-difference scheme is used with standard 2^{nd}-order and 4^{th}-order artificial dissipation terms for the near-body grids. Baldwin-Barth turbulence model was used. The off-body grids also use the 4^{th}-order spatial central-difference scheme but with inviscid flow modeling to minimize wake dissipation. A 1^{st}-order temporal scheme was used with a time-step of 0.05 degrees (7200 steps per rotor revolution) to ensure numerical stability.

Fluid/Structures Interface

The Fluid/Structures Interface (FSI) framework used to couple the CFD model with rotorcraft comprehensive analysis is described in detail in Ref. 5. The central idea was to provide blade elastic deflections from the comprehensive analysis to the CFD solver and the aerodynamic forces computed by CFD back to the comprehensive analysis. This data exchange is done through file i/o to maintain code modularity. The loose coupling (LC)

algorithm first developed by Tung *et al.* (Ref. 16) is used for periodic solutions. For maneuver calculations, the tight coupling (TC) algorithm is used where the deflections and airloads are exchanged at every time step. At present, a "lagged" scheme is employed where the comprehensive analysis (i.e., the structural solution) precedes the CFD solution by one time-step. The deflections at the new time-step are calculated using the CFD airloads from the previous time-step in an explicit manner. The new deflections are then provided to the CFD solver and new forces are computed. Since the time-step used in the current study is small, the time-lag between the two solvers is not a significant concern.

Original FSI implementation transferred only the normal force, chordwise force and pitching moment from the CFD solver. This was readily extended to include all six force and moment components. An interpolation/integration scheme was developed to ensure that the loads transfered from OVERFLOW-2 to RCAS are consistent in an integral sense. To achieve this the CFD airloads are integrated over the RCAS spanwise aerodynamic segments, rather than simply interpolating the values to the RCAS aerodynamic control points (ACPs). This is schematically described in Fig. 3 where an example CFD normal force distribution and the RCAS blade aerodynamic segments are shown. The airload at the ACP is determined by integrating the CFD airloads over the corresponding segment as shown by the shaded area under the normal force curve. This is essentially a simple conservative finite element interpolation scheme (Ref. 17) with a constant load distribution over the aerodynamic segments. This scheme is used for all the six airloads components and gives a less than 0.5% discrepancy between the integrated CFD airloads and the airloads seen by RCAS blade model.

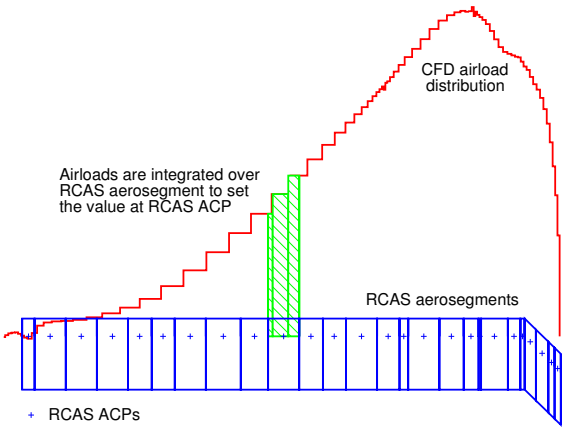

Fig. 3. Integration/interpolation to transfer CFD airloads from OVERFLOW-2 to RCAS ensuring that the integrated loads are conserved

The FSI framework was extended to exchange not only the airloads and blade deflections but also the flight conditions between RCAS and OVERFLOW-2. The vehicle global frame motions are incorporated into the CFD flow solver through the FSI using the orientation and velocities of the RCAS vehicle frame. The vehicle angular rates during a maneuver directly translate into an equivalent velocity seen by each of the grid points (cross product of the angular rates and distance from rotation center). In addition to this, the effective freestream velocity in the CFD system may need to be changed with time as the vehicle orientation changes. This is achieved by adding grid speeds to the time metrics in the flow solver. The difference between the equivalent air speed in the RCAS vehicle frame (translational velocity minus physical wind velocity) and the freestream velocity in CFD is added to the time metrics. Essentially, this process mimics the RCAS vehicle orientation changes in CFD by correspondingly changing the freestream velocity such that the net incoming flow seen by the vehicle (or rotor) is identical in both RCAS and OVERFLOW-2 solutions.

The RCAS and OVERFLOW-2 coordinate systems along with the UH-60A models are shown in Fig. 4. The OVERFLOW-2 coordinates are a Cartesian system with the x-axis pointed aft, y-axis to the right and z-axis up. RCAS uses several coordinate systems, with each component and elements having their own coordinate systems. Each of these systems can be readily related to the inertial system through transformation matrices. The vehicle global system (G-frame) is typically attached to the fuselage near the aircraft center of mass. The inertial system is fixed with the z-axis pointing downward. The x-axis points north by convention and in the example shown, the aircraft has a heading of about 105 deg (at the beginning of the UTTAS pull-up). As the coordinate transformations are readily available in RCAS, it is easy to supply the CFD solver with the shaft orientation, vehicle velocity and the wind velocity in the inertial-frame. Although the RCAS vehicle frame may change orientation during a maneuver, the relationship between the CFD-system and the RCAS inertial system is also known through user-specified inputs describing the CFD system origin and initial orientation in the CSD system. With this information, OVERFLOW-2 can calculate the grid speeds necessary to ensure that the relative flow speed seen by the rotor is the same in both models.

The grid speed to be added to each CFD grid point to ensure a consistent flowfield between the RCAS and OVERFLOW-2 models are given by

$$V_{\text{maneuver}} = V_{\infty,\text{CFD}} - V_{\text{wind,CSD}} + V_{\text{translation,CSD}} + V_{\text{rotation,CSD}}$$

where all of the velocity components are expressed in the CFD coordinate system.

In maneuvering flight, this approach is essential to provide the time-dependent vehicle translation and rotational motions from RCAS to CFD. Even for trim calculations with LC, this approach ensures that the correct flight conditions like roll/pitch attitudes from RCAS are

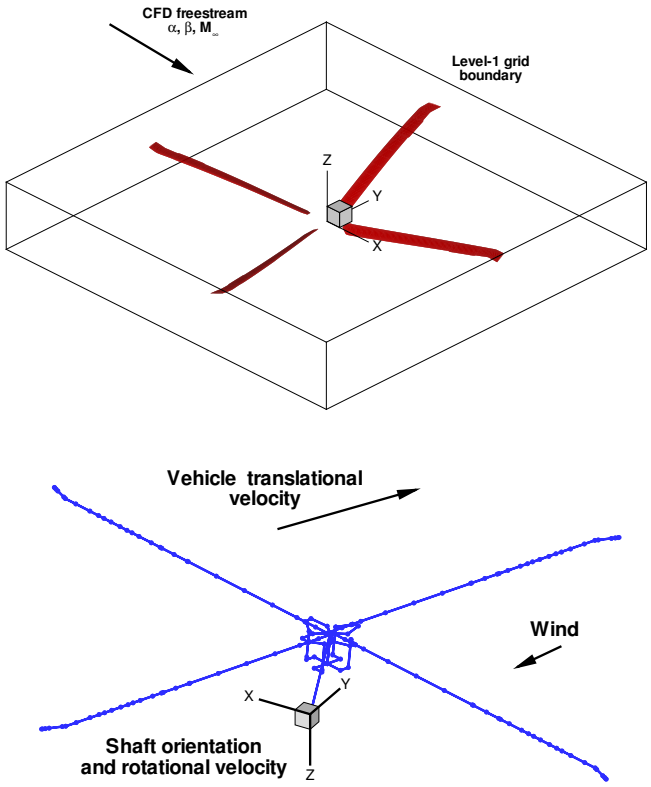

Fig. 4. Relating the OVERFLOW-2 and RCAS coordinate systems and vehicle/flow velocities

conveyed to the CFD solver. For example, in full aircraft (6-DOF) trim, the roll/yaw attitude of the aircraft may change as the trim solution progresses and will be different from the initial conditions set in the CFD flow solver. With this extended FSI implementation, the flow conditions in CFD are correctly set using the RCAS flight conditions, rather than the original CFD inputs. This grid speed approach avoids having to reorient the complete CFD grid geometry, which might result in the need for off-body re-meshing/adaption.

Validation of the RCAS/OVERFLOW-2 FSI

Maneuver calculations were started from a well-converged LC trim solution for steady level flight. An example of this transition from LC to TC is shown in Fig. 5, where blade normal force coefficient at 77% radial station is shown as a function of time (blade azimuth) for both LC and TC calculations. No control input changes were applied during the calculation and, therefore, the rotor should, and does, remain in trim. This is readily seen in Fig. 5 where the TC results for the four individual blades closely follow the LC result (which is identical for all four blades). The small blade-to-blade differences seen in the TC solution are because the four blades in the CFD solution are converged to the same periodic solution with a small tolerance. Nevertheless, these differences are small enough not to affect the maneuver calculations, and can be easily reduced further by increasing the number of revolutions of the LC solution.

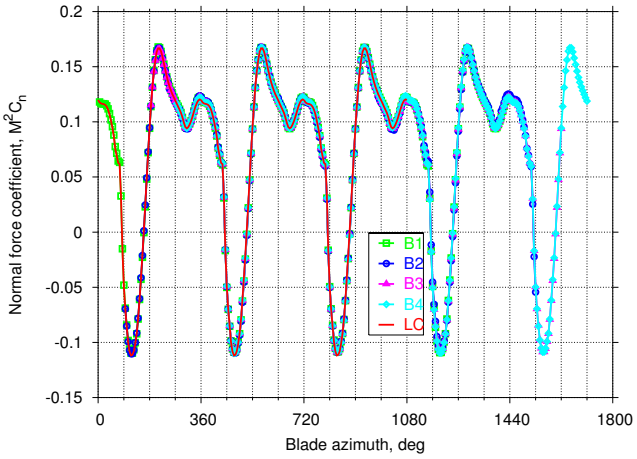

Fig. 5. A time-accurate TC solution started from converged periodic LC solution (trim)

To exercise and validate this time-accurate TC maneuver capability, a simple test problem was set up to calculate the rotor response to a vertical translation excitation and an equivalent vertical wind gust. The aircraft in steady level flight moves downward at a constant 20 fps rate over a quarter rotor revolution and then moves up at the same rate over the next quarter revolution. This is equivalent to the aircraft encountering a vertical gust of the same magnitude but opposite direction as shown in Fig. 6. If the rotor is completely rigid, then these two excitations are equivalent and would show identical responses. The calculations for these two cases are shown in Fig. 6(a) as the perturbation normal force coefficients at 77% spanwise station. The two responses are identical with an initial increase in normal force as the gust/vehicle motion reduces the inflow seen by the rotor. The transient response quickly diminishes because the rotor is rigid. For a flexible rotor, however, the two excitations are not equivalent, as can be seen from Fig. 6(b). At the 77% spanwise station, the effect of the gust is seen immediately with an initial increase in normal force. On the other hand, the vehicle motion applied at the hub is felt at the 77% span station only after some time because of the blade elastic dynamics. As a result, the responses to the two excitations are significantly different.

Another important aspect of the time-accurate TC approach is the ability to save and restart a run. The maneuver calculations presented in this study span over forty rotor revolutions. Computational job/queue limitations make it impractical to run the entire coupled maneuver calculation as a single run. Typically it is broken into several runs spanning four rotor revolutions each. At the end of each run both RCAS and OVERFLOW-2 save some restart files, which are used in the subsequent run. It is imperative that the time-accurate calculations do not introduce any numerical transients as an artifact of the restart process between two such runs. To ver-

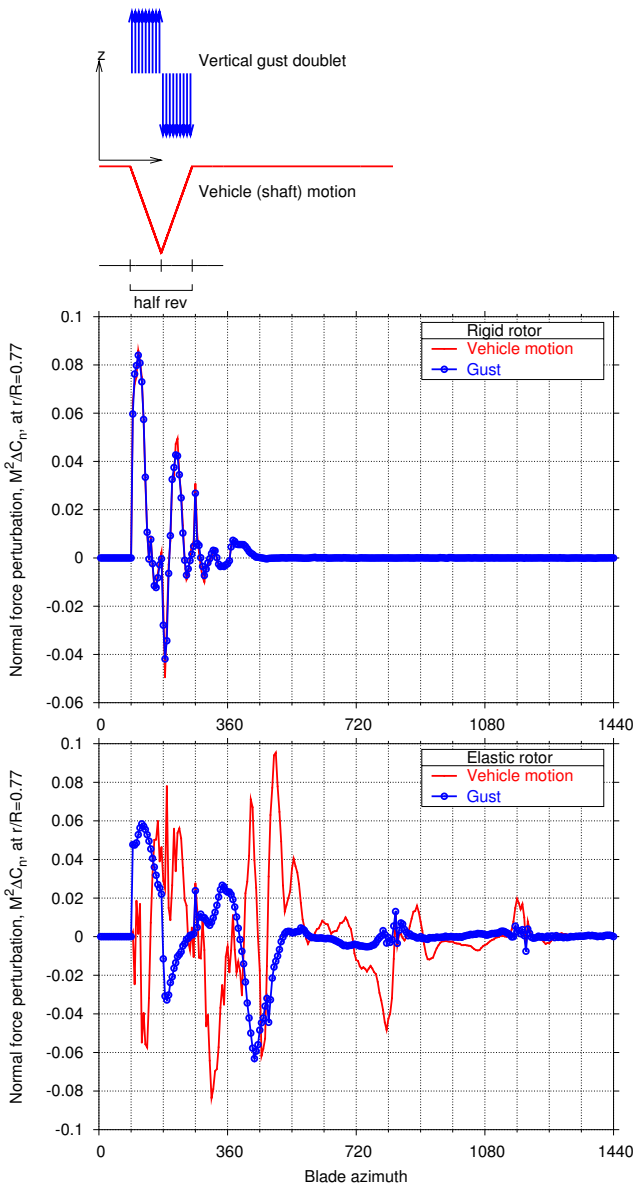

Fig. 6. Response to vertical gust/plunge (a) Rigid rotor, (b) Flexible rotor

ify this, example calculations were run where one long run was broken into two pieces. Computed rotor aerodynamic thrust is shown in Fig. 7 as a function of time (rotor revolution). The two-part calculations are identical to the single run demonstrating a seamless restart.

The UTTAS Maneuver

The principal focus of the paper is the analysis of the UH-60A UTTAS pull-up maneuver performed during the NASA/Army UH-60A Airloads Program. The maneuver and relevant data acquisition procedures will be briefly described. After an brief period to stabilize the 158 knots high-speed, level flight initial condition, an aggressive maneuver was initiated that achieved a 2.1g normal load factor within approximately two sec. The pull-up was

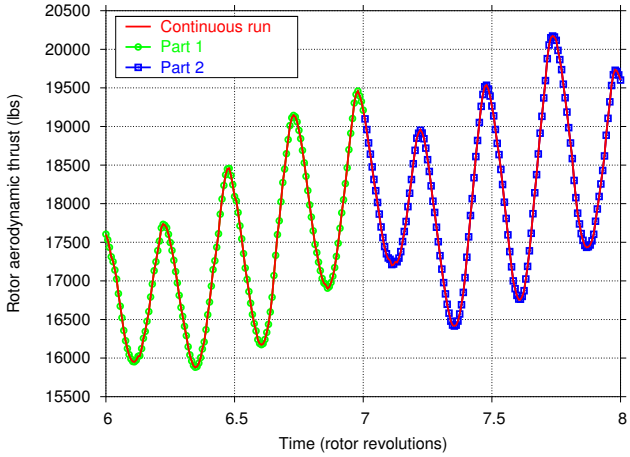

Fig. 7. Restarting RCAS/OVERFLOW-2 TC calculations in the middle of a maneuver

executed primarily as a longitudinal maneuver and concluded with a pushover recovery. After 40 rotor revolutions the aircraft returned to roughly 0.65g normal load factor with the entire maneuver lasting about 9.5 sec.

The data measured during the flight test program were processed and recorded as a function of time in the TRENDS database system. Data for the UTTAS pull-up maneuver, counter 11029, were subsequently downloaded in Plot/Database (P/DB) files.Each revolution was downloaded as a separate P/DB file; those were later concatenated into a single file for the entire 40 rev maneuver time history. The files included the following parameters: blade airloads consisting of airfoil section normal force, chord force, and pitching moment for nine blade radial locations based on integrated blade surface pressures; blade loads and motion data consisting of flatwise and edgewise bending and torsion structural loads, pushrod and damper loads, rotor shaft torque and bending moment, and blade pitch, flap, and lag hinge motion; and the aircraft motion data, including linear and angular position, velocity, and acceleration of the vehicle center of mass. All of this data was used either as input to define the maneuver analysis, or to compare with results produced by the RCAS and OVERFLOW-2 maneuver analyses.

In order to understand the details of the UTTAS pull-up, time histories of the principal maneuver parameters will be described in the following figures. The normal load factor in g, and the angle of attack, α, pitch attitude, θ, and flight path angle, γ, in degrees are all presented in Fig. 8. The initial period of steady-state level flight extends for about four rotor revolutions before the aft longitudinal cyclic input is initiated. A small discrepancy (approximately 3 deg.) in vehicle angle of attack and pitch attitude is present; strictly speaking, in level flight, angle of attack and pitch attitude should be identical. It is surmised that the angle of attack measurement may be influenced by the fuselage and rotor flowfield in high speed flight even though the sensor vane is located well

ahead of the nose of the aircraft (see Fig. 1).

Following the initiation of the cyclic control input, the rotor thrust and normal load factor responses slightly precede the angle of attack and pitch attitude response. The $2.1g$ peak normal load factor is achieved during revs 15–17 followed by peak pitch angle and angle of attack of roughly 30 and 10 deg. respectively at rev 19. The aft cyclic input is removed at rev 17 and normal load factor diminishes to 1.0 and then 0.65 at the end of the record at rev 40. Pitch attitude recovers to 10 deg., at rev 40 but the flight path angle is still at 30 deg., consequently, the aircraft is at a peak 20 deg. negative angle of attack! Full recovery to steady level flight does not occur for another 30 or so revs but the maneuver analysis does not extend beyond 40 revs.

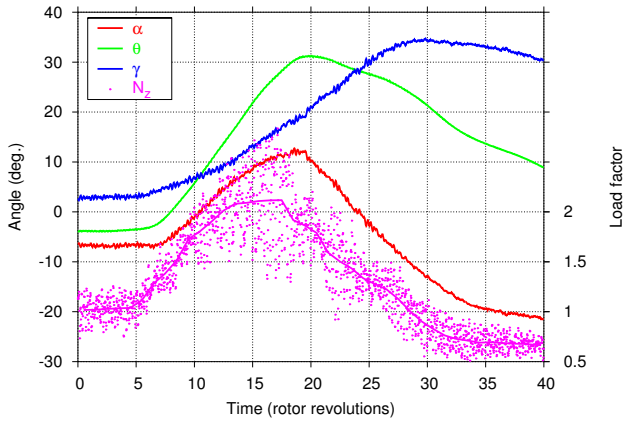

Fig. 8. Aircraft aerodynamic angle-of-attack, α, pitch attitude, θ, and flight-path angle, γ, along with normal load factor, n_Z

The associated pitch, roll, and yaw rates, (p, q, r), are presented in Fig. 9, and the sideslip, β, roll, ϕ, and yaw, $\Delta\psi$, angle excursions are presented in Fig. 10. These measurements show that the maneuver was primarily a longitudinal pull-up, but moderate lateral responses occurred, not unexpected given the high speed flight condition and the aggressiveness of the maneuver. Finally, Fig. 11 shows the variations in rotor speed and aircraft velocity and the altitude gained during the maneuver. The airspeed decreased by 38% while the rotor speed remained nearly constant with momentary deviations on the order of 1%. Advance ratio decreased from 0.36 to 0.22. At the end of the data record, the aircraft had gained several hundred feet of altitude and was still in climbing flight. Calculated vehicle vertical (z) position is also shown for comparison.

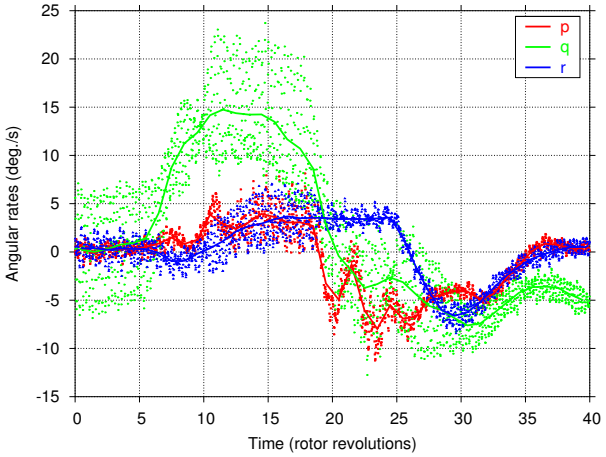

Fig. 9. Pitch, roll and yaw rates, (p, q, r)

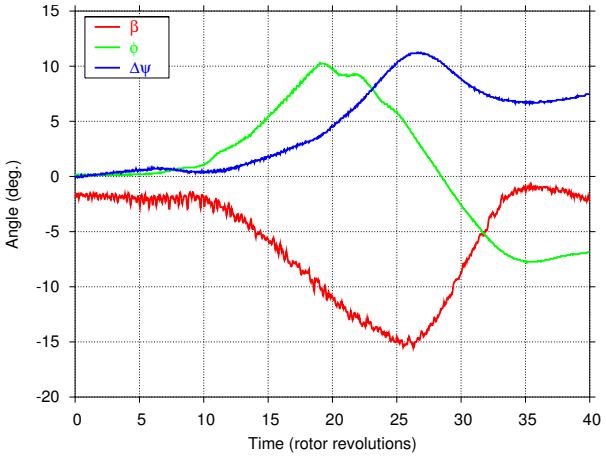

Fig. 10. Sideslip, β, roll, ϕ and yaw angle, $\Delta\psi$

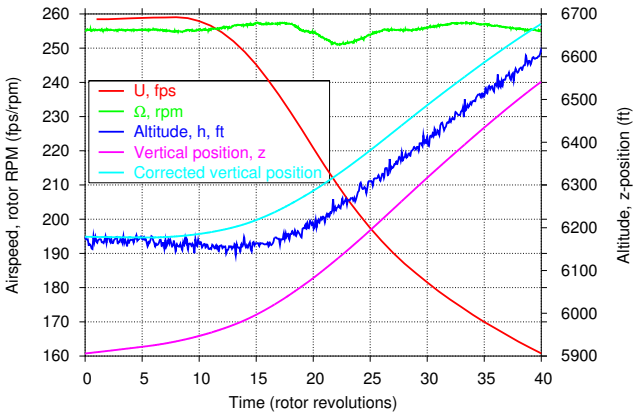

Fig. 11. Airspeed, U, rotor speed, Ω, pressure altitude , h and the calculated vehicle input vertical (z) position

Maneuver Analysis

The RCAS code enables a variety of maneuver analyses — nonlinear transient responses to input variables — to be performed in the time domain. Typically, but not necessarily, these analyses are preceded by a trim analysis to determine control variables to satisfy appropriate trim constraints. A full free-flight maneuver would involve flight dynamic and aeroelastic response of a complete rotorcraft to time varying pilot control inputs. For the UTTAS pull-up maneuver of this paper, the analysis is limited to the calculation the aerodynamic and dynamic

responses of the four main rotor blades to prescribed rotor pitch control and hub motion inputs measured during the flight test. Using the experimentally measured vehicle motion insures more consistency than a full free-flight maneuver analysis since the airload and blade loads comparisons will correspond more closely to the same rotor operating conditions.

For the present RCAS maneuver analysis, the input consists of the time history of 21 rotor pitch control and rotor motion parameters. The three rotor controls are the collective, lateral cyclic, and longitudinal cyclic pitch, and the motion inputs are the 18 linear and angular position, velocity, and acceleration components of the rotorcraft with respect to inertial space. In RCAS, the reference frame for defining vehicle motion is the G-frame that is usually located near the nominal center of mass of the vehicle. The motion at rotor hub reflects the G-frame motion and the location of the rotor hub with respect to the G-frame origin.

Vehicle Motion Input Data

The G-frame motions for the RCAS maneuver analysis were obtained from the flight test measured vehicle motion parameters as follows. The measured vehicle velocity was combined with the angle of attack and sideslip angle to calculate the three velocity components in vehicle body axes. These were transformed using the measured body roll, pitch, and yaw orientations to yield linear velocities in inertial space. Similarly, the angular velocities in inertial coordinates were obtained from angular velocities measured in vehicle body coordinates. Likewise, linear and angular accelerations with respect to inertial space were determined. The calculated vertical motion is compared with the measured vertical position (from barometric pressure) in Fig. 11. The results show large differences because of the initial climb angle discrepancy discussed earlier. After including adjustments made for the initial climb angle discrepancy discussed earlier, the results are reasonably consistent. However, this small climb rate implies a larger rotor torque (see later).

Rotor Pitch Control Input Data

The rotor blade pitch control input data time history is important to accurately calculate rotor response. In steady flight, the periodic motions of each blade are identical and a single blade's pitch angle is sufficient to define the rotor collective and cyclic pitch. During a transient maneuver, the blade motions are neither the same nor periodic; consequently collective and cyclic pitch are time varying and depend on the pitch of each blade.

During the UH-60A flight tests, motion of each of the four blades was measured with specially designed instrumentation. The flapping, lead-lag, and pitch motion of the blade root is defined by rotations of the blade spherical elastomeric pitch bearing. These rotations were indirectly measured by a mechanical apparatus known as blade motion hardware (BMH) consisting of a system of links and rotary transducers. The blade pitch, flap, and lead-lag, angles were obtained from a nonlinear transformation of the BMH angle measurements. Since the transformation related all three BMH angles to all three blade motion angles, experimental error in a single BMH angle measurement propagated to all three transformed blade angles.

In fact, several of the BMH angle data records for counter 11029 contained significant measurement errors for blades 1 and 4. Consequently, the rotor collective and cyclic pitch input time histories were based on only the blade 2 and 3 pitch angles. This reduced the accuracy of the higher frequency content of the collective and cyclic pitch, but this is probably not of great importance given the relatively slow time scale of the maneuver. In addition to these issues, the resultant rotor control angles were inconsistent with the equilibrium flight condition for the steady-state level flight portion of the maneuver preceding the pull-up. Therefore adjustments were made to the three rotor pitch controls based on trim solutions obtained with RCAS and OVERFLOW-RCAS computations. These adjustments were then added to the maneuver control input time history. Figure 12 shows the adjusted control time histories that were used for the maneuver analyses along with the unadjusted measurements. The OVERFLOW-RCAS and RCAS adjustments differ primarily because of the differences in the rotor wake modeling.

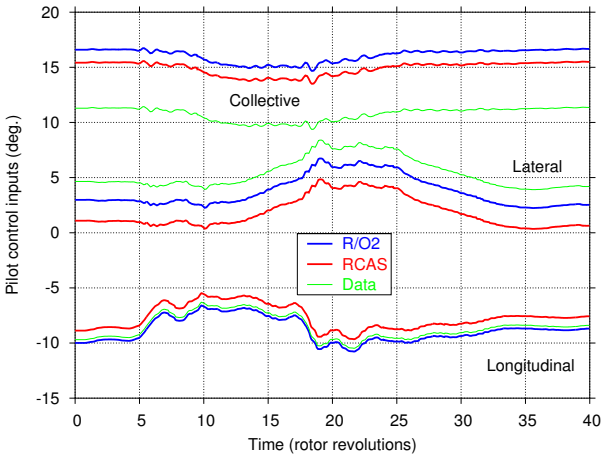

Fig. 12. Pilot control inputs: measured and computational inputs for RCAS and RCAS/O2

Maneuver Analysis Results

Before computational results are presented, the different analyses that were conducted will be briefly discussed. Three separate analysis categories are included.

Analysis Overview

The standard maneuver analysis for RCAS without coupling to the CFD code typically involves performing the trim solution to determine rotor controls in steady state flight. First, a separate three-DOF trim solution yielded the rotor collective and cyclic controls that satisfied trim targets for rotor thrust, pitch, and roll moments. The maneuver was performed in a second run where the input time history for controls and G-frame motions were loaded from a file and two separate analyses sequentially performed using RCAS `useradditionalpretrim` and `useradditionalanalysis` scripts tailored to the specifics of the UTTAS pull-up maneuver. The first script initialized the periodic solution using inputs for the first maneuver time step and the second script executed the transient maneuver for the full maneuver time history. The time step size was typically 72 time steps per revolution (5 deg. azimuth).

The second maneuver analysis was performed to calculate the rotor forces and blade structural loads in response to the flight test measured blade airloads. This so-called mechanical airloads (Ref. 11), or measured airloads, analysis was primarily performed to determine the net rotor thrust from integration of the measured airloads over the rotor disk. Accurate integration of the normal and chordwise forces and the pitch moment airload distributions requires simultaneous calculation of the blade elastic deflections to properly orient the blade airloads, therefore a full aeroelastic maneuver analysis using the measured airloads was conducted. Even for steady-state conditions, the mechanical airloads analysis is subject to unique accuracy issues associated with structural dynamics response of lightly damped systems (Refs. 11,12) and some of these issues were encountered during the present analysis. However, reasonable results were obtained for the rotor thrust.

The third, and principal analysis, was the coupled RCAS/OVERFLOW-2 maneuver analysis. The maneuver analysis was initiated from a LC trim calculation. The trim targets for this case were same as those for the counter 8534, but the vehicle initial conditions (orientation, velocity) were set using the initial time step of the maneuver time history. The maneuver calculations were started using this LC solution as initial condition for both RCAS and OVERFLOW-2. The maneuver pilot control inputs were adjusted to match the trim pilot inputs — see the shift between analysis inputs and data in Fig. 12. The calculation was split into four-revolution pieces and each run used restart information for both RCAS and OVERFLOW-2 from the previous run. To examine the validity of the LC approach during the maneuver three revolutions where the load-factor was close to maximum were calculated using a quasi-steady LC approach. In this case, the inputs were averaged over one rotor revolution and held constant (accelerations were set to zero).

Computational results will now be presented for the UTTAS pull-up maneuver. Results will include rotor hub force and moment reactions (thrust & shaft torque, upper shaft bending moment), detailed blade airloads predictions and then progress to blade structural loads. Results will be compared with measured data in most cases and conventional RCAS results will be included for comparison as appropriate.

Unless otherwise noted, the baseline results use the nonlinear damper, the stiff pushrod, and the pitch bearing damping of 20 $\text{lb-ft}/\text{rad}/\text{sec}$. The baseline RCAS results use the uniform inflow wake and Leishman-Beddoes dynamic stall model. Note that because of the simple wake model, this should not be considered a state-of-the-art lifting-line calculation. The full maneuver RCAS results include all 40 rotor revolutions, the full maneuver for the RCAS/OVERFLOW-2 results include the first 24 rotor revolutions.

Rotor Hub Vertical Force

The first results examine the overall rotor thrust and moment characteristics during the UH-60A UTTAS pull-up maneuver including the influence of several aerodynamic and modeling variations.

The rotor hub vertical force calculated by both RCAS/OVERFLOW-2 coupled analysis (denoted as R/O2 for brevity) and RCAS alone during the pull-up maneuver is shown in Fig. 13. This is the net hub force in the rotor shaft direction, F_Z, and includes the force of the blade weight and the maneuver load factor. The initial thrust force is for trimmed flight; thrust equals vehicle weight plus estimated fuselage and tail download. The maneuver thrust variation with time, plotted in units of rotor revolution, shows the thrust increase and decrease during the pull-up. The vibratory thrust oscillations are caused by the unsteady aerodynamics as well as inertial reactions to the G-frame acceleration inputs. The thrust oscillations are primarily 4/rev along with some 1/rev content. The R/O2 and RCAS results are very similar during first ten revs of the maneuver but begin to depart thereafter; notably, the R/O2 maximum thrust exceeds the maximum RCAS thrust by roughly 3000 lbs. As the thrust decreases, the difference diminishes and the two results converge around the 24^{th} rev. It appears that the RCAS conventional aerodynamic modeling produces an earlier rotor stall than the OVERFLOW-2 CFD aerodynamics modeling.

Since the rotor thrust was not directly measured during the UH-60A Airloads Program, it is not possible to directly evaluate the accuracy of the calculated rotor thrust. However, there are two ways to indirectly check the analysis, first from the normal load factor and second from the integrated blade pressure measurements. As discussed earlier, the mechanical airloads analysis provided an integration of the measured airloads for the

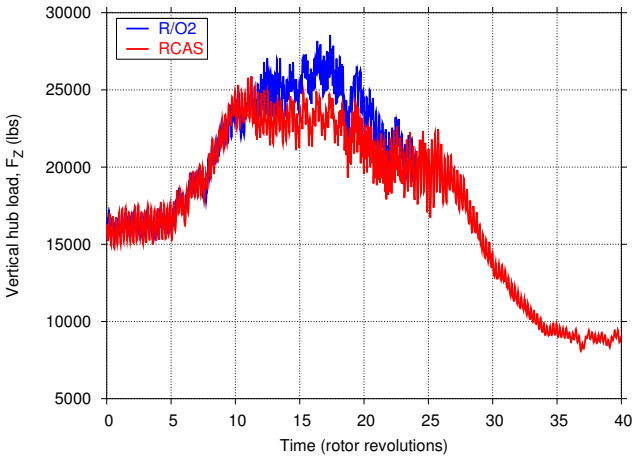

Fig. 13. Calculated hub vertical force

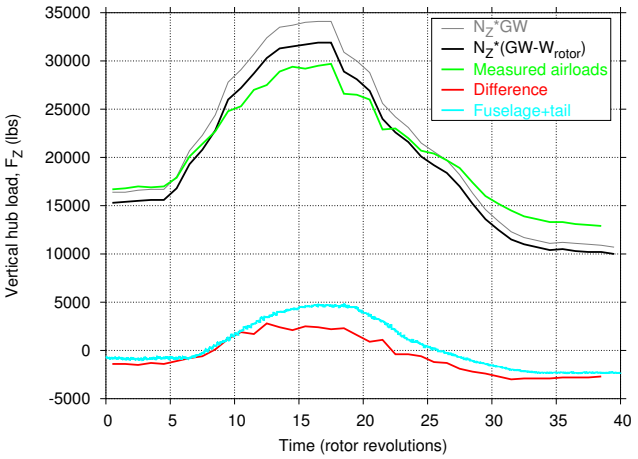

Fig. 14. Vertical forces balance during the maneuver using measured airloads

rotor thrust force and shaft torque. One more component of the vertical force equilibrium that must be included is the contribution of the fuselage and horizontal tail. These contributions are calculated using an empirical model for the UH-60A fuselage and tail commonly used in fixed-based simulations. It represents fuselage aerodynamics with a data table of coefficients parameterized by angle of attack and sideslip. Horizontal tail forces are based on lifting line theory and include the measured tail incidence time history. These results will now be compared as a check on the equilibrium of the component forces acting in the rotor shaft direction.

The first comparison (Figure 14) presents the force balance based on the measured airloads of the rotor for the full 40 rev maneuver time history. Integrated airloads result is presented in terms of the per-rev average measured airload. The figure also includes the calculated fuselage and horizontal tail lift and it is clear that this force is significant, varying from about 1700 lbs download in trim flight to a maximum of nearly 5000 lbs, a net difference of close to 7000 lbs. This represents roughly 20% of the maneuvering lift. Ideally, the fuselage and tail force would be equal to the difference between the total vehicle force and the rotor force (also included in Fig. 14), however, either this force is overpredicted, or the integrated airload measurement is too high. If previous experience is considered accurate (Ref. 2), it would be appropriate to reduce the integrated measured airloads by 7-10%, in which case all three thrust constituents would be in good agreement, including the variation as a function of time.

The second result in Fig. 15 repeats the force balance comparison using the R/O2 and RCAS thrust calculations. The thrust data from Fig. 13 is here converted to the per-rev averages. The rotor thrust and vehicle total force include the rotor weight and inertial forces. Here again, the force balance results are quite reasonable, except perhaps at the end of the maneuver from revs 30–40 where the predicted result predicted by RCAS decreases below the total vehicle force implying an unrealistic positive thrust contribution from the fuselage and tail. Since RCAS and OVERFLOW are in good agreement during the first part of the maneuver, before the highest thrust region, it is expected that OVERFLOW would experience the same discrepancy for revs 30–40. It is hypothesized that this discrepancy may be the result of inaccuracies in the rotor controls or vehicle motion maneuver input history. One final note is that the thrust capability of conventional aerodynamic methods, as manifested by the RCAS results, is deficient by approximately 3000 lbs in supplying the rotor thrust needed to achieve the the $2.1g$ normal load factor of the UTTAS pull-up maneuver.

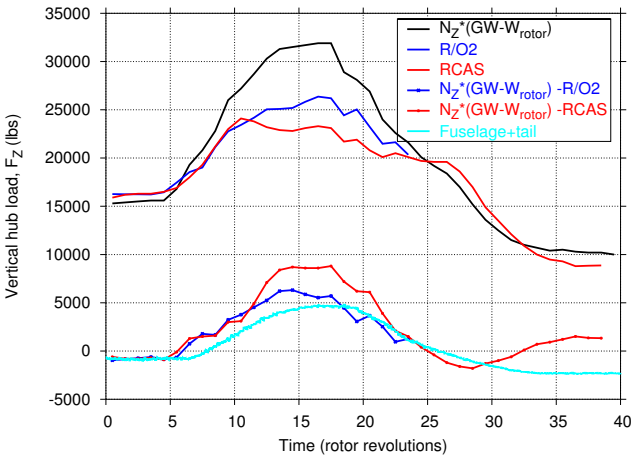

Fig. 15. Vertical forces balance during the maneuver using computed loads

Rotor Hub Shaft Torque

The rotor shaft torque calculated by R/O2 and RCAS during the pull-up maneuver is shown in Fig. 16. Here, direct shaft torque measurements are also available. The calculated and measured results are in general agreement but differ in a number of areas. During the pull-up, the torque decreases as the shaft angle of attack increases and

the rotor operating state shifts in the direction of autorotation. The calculated results overpredict both the initial steady-state torque and the reduction in shaft torque during the pull-up. The initial overprediction may be related to the discrepancy in flight path angle present in the G-frame motion input during the steady-state part of the maneuver. In addition, the shaft torque prediction is sensitive to airfoil drag characteristics especially for stalled conditions. Also evident in the shaft torque calculations are low frequency transient responses. These are manifestations of the blade fundamental lead-lag mode that has a natural frequency near 0.3 per rev. Maneuver excitations due to the G-frame angular accelerations as well as control input variations easily excite responses of this mode and these appear as lightly damped shaft torque reactions.

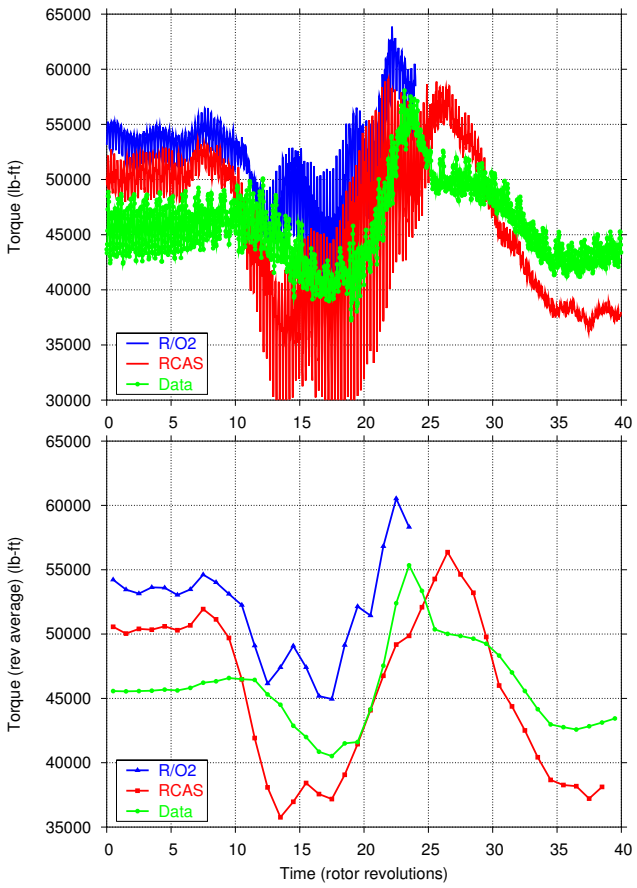

Fig. 16. Main rotor torque

The 4/rev vibratory shaft torque amplitude is roughly similar to the measured vibratory torque level. This will be sensitive to the impedance, or dynamic coupling, of the rotor drive train system that is not included in the RCAS structural dynamics modeling for this problem.

Rotor Shaft Bending Moments

Rotor hub pitch and roll moments are basic flight dynamics parameters that reflect the interplay between pilot control inputs, pitch rate, and vehicle angle of attack response that determine the trajectory and normal load factor of the pull-up maneuver. The hub moments are measured indirectly as bending moments of the rotor shaft just below the rotor hub. This upper shaft bending moment is measured in the rotating system and, since only one of two orthogonal components is available, the fixed system pitch and roll moments cannot be determined (for unsteady conditions) by resolving the two shaft bending moment components in the rotating system. Nevertheless the single shaft bending moment component can be compared with the predicted result as shown in Fig. 17. Figure 17(a) compares the time history for the first 24 revs of the R/O2 result with test data. Figure 17(b) shows the corresponding per rev 1/2 peak-to-peak (1/2-PTP) comparison. The predominant 1/rev response of the shaft bending moment implies a steady hub moment proportional to the waveform amplitude with the pitch/roll components determined by the waveform phase. The predicted results, both 1/2-PTP as well as the waveforms are in general qualitative agreement with the test data up until the peak load factor before the amplitude and waveform comparisons begin to significantly depart. In fact the measured hub moments become very small and the waveforms very distorted, indicative of an unexplained change in the rotor response behavior. Similar behavior will be observed later for the blade flapping results, not surprisingly since the rotor hub moments are directly related to rotor blade flapping angle.

Rotor Blade Motion

Blade pitch angles are compared in Fig. 18 for Blade 2 showing both the waveform time histories and the 1/2-PTP amplitudes. The differences include the collective and cyclic adjustments applied to the maneuver input history and the small difference between the control input applied to the base of the pushrod and the calculated pitch angles at the pitch hinge that reflect the effect of pushrod elastic deflections.

Blade flapping angles during the maneuver are compared for Blade 2 in Fig. 19 again showing both the waveform time histories and the 1/2-PTP amplitudes. As noted above, there are strong similarities to the rotor shaft bending moments comparisons shown in Fig. 17. During steady-state level flight, the R/O2 and RCAS results are similar to the test measurements for both waveforms and cyclic amplitude. During the pull-up maneuver, all three flapping angles diverge. The R/O2 cyclic amplitude over-predicts the measured flap angle while the RCAS result under-predicts it initially. Interestingly, the RCAS and R/O2 results mainly differ only from revs 10 to 20, the same time period where RCAS thrust could not match the R/O2 thrust (see Fig. 13).

The implication of this is that blade stall may well

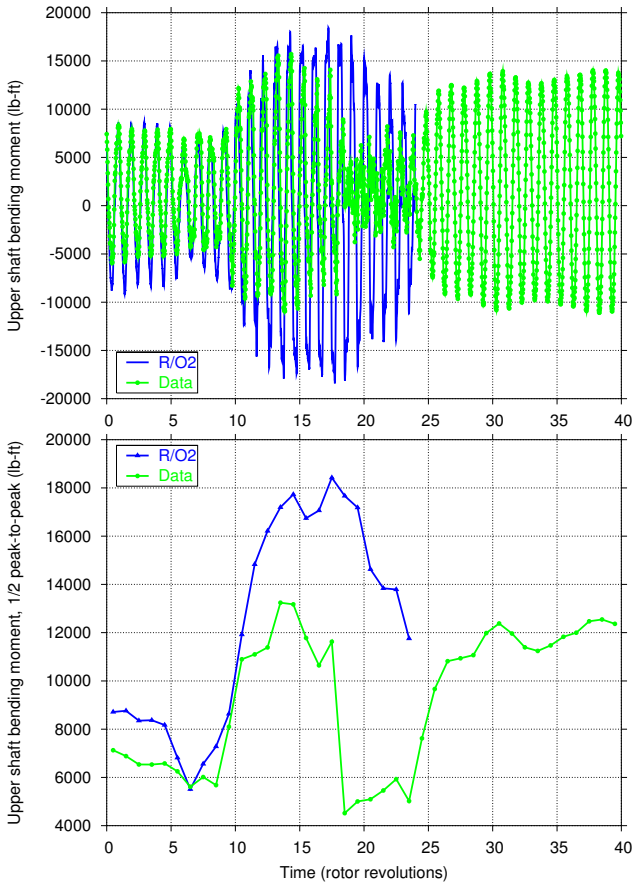

Fig. 17. Rotor shaft bending moment

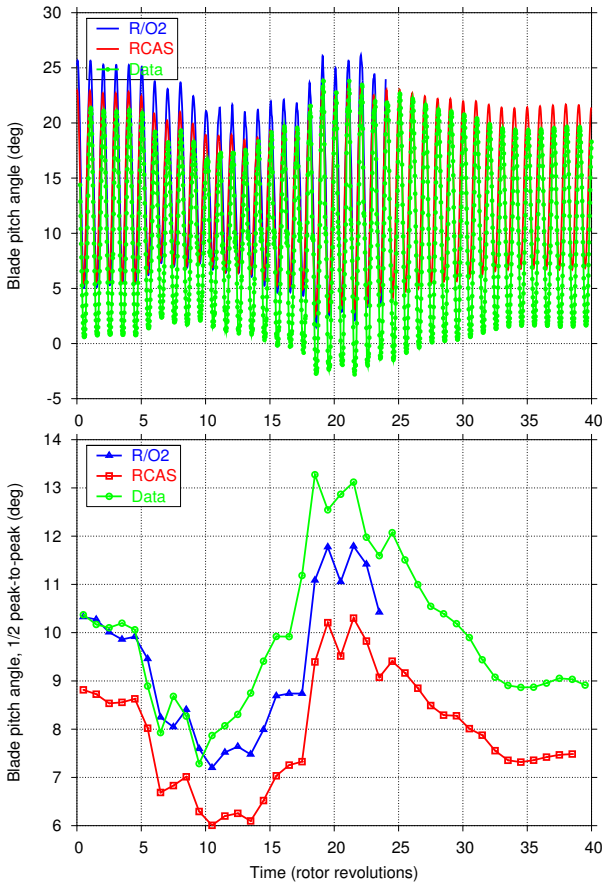

Fig. 18. Blade #2 pitch angle

be influencing the blade flapping. Unusual behavior occurs between revs 20 to 30. Near rev 20, the experimental blade flapping amplitude diminishes significantly, the waveform becomes distorted with a predominant 2/rev content. Similar changes occur for the RCAS flapping angle near rev 26. Other differences are also evident for flapping phase that reflect variations of the rotor tip-path-plane angle throughout the maneuver from forward tilt in level flight to aft tilt during the pull-up and back to forward tilt as the vehicle angle of attack becomes negative during the recovery to level flight. The 1/2-PTP variations for flapping of all four blades is shown to highlight blade-to-blade differences. Some of the differences between calculated and measured flapping angle can be attributed to measurement errors associated with the BMH instrumentation discussed above although it must be noted that the flapping angle behavior is strongly correlated with the rotor shaft bending moment. Another explanation for the differences could be inaccuracies in the maneuver control and motion inputs — clearly, these would introduce errors in the blade flapping responses.

Finally, representative blade lead-lag angle responses are compared in Fig. 20 for Blade 2. The general features of the lead-lag angle maneuver response is very similar to the rotor shaft torque response as would be expected. For these results, the R/O2 predictions compare more closely with the flight test measurements than the RCAS results. Again, some of the differences between predictions and test data, as well as blade-to-blade variations, can be attributed to the BMH instrumentation issues.

Maneuver Thrust Augmentation

The R/O2 results for rotor thrust have been shown to be generally consistent with the total vertical force balance of the aircraft at the $2.1g$ peak load factor of the maneuver. This level of rotor thrust substantially exceeds the steady state McHugh rotor thrust boundary, and thus it is of interest to understand how the rotor thrust can be augmented in the maneuver condition. Accounting for the effects of fuselage and tail lift, the maneuver thrust augmentation is approximately 15% at the peak load factor. It is also of interest to understand why the RCAS peak rotor thrust is significantly less than the R/O2 thrust capability.

It has been suggested that an increase in maximum rotor thrust capability in maneuvering flight results from the pitch-rate-induced gyroscopic roll moment associated with the positive pitch rate of the aircraft during the pullup. Moment equilibrium in the roll axis requires that an external moment be provided to balance the gyroscopic moment and this can only be produced by the rotor blade normal force airloads. The direction of the roll

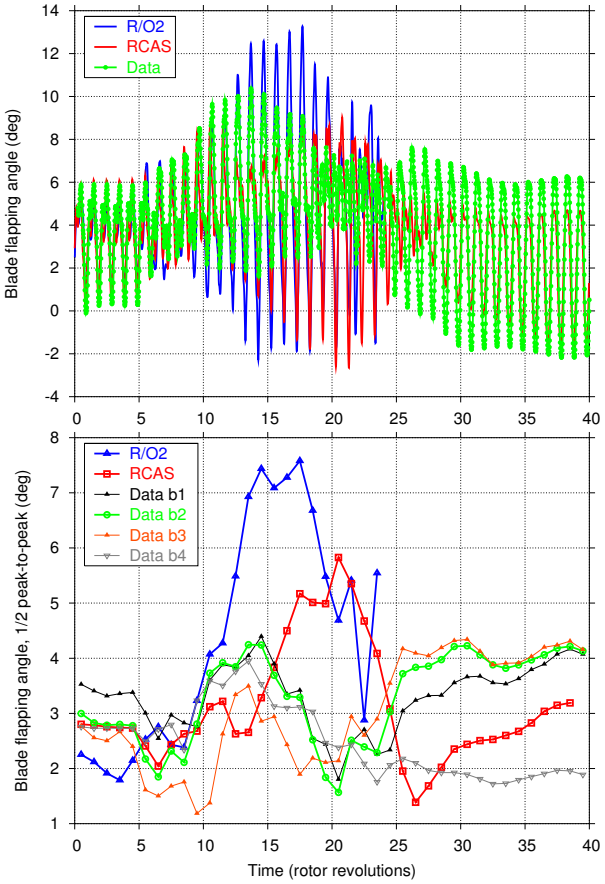

Fig. 19. Blade #2 flap angle

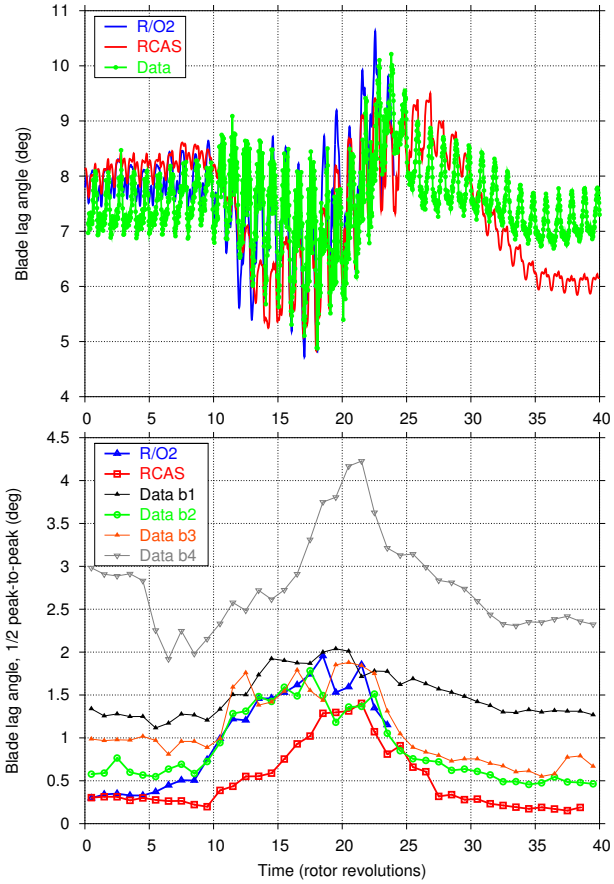

Fig. 20. Blade #2 lag angle

moment requires the advancing blade to increase lift and the retreating blade to reduce lift and fortuitously this relieves the lift requirement of the retreating blade. This translates into increased stall margin — that is, the rotor can produce more thrust before reaching the retreating blade stall limit.

This was checked by running the RCAS maneuver analysis without the G-frame angular velocities. The result was a reduction in peak thrust of approximately 3000 lbs (implied 12.5% thrust augmentation) and increase in aft rotor tip-path-plane tilt as would be expected.

RCAS and conventional aerodynamics predicted lower rotor thrust during the maneuver than R/O2 when significant blade airfoil stall was present. It is sometimes argued that unsteady phenomena occurring during the transient maneuver would enable the rotor airfoil stall to be delayed to higher lift levels and possibly generate higher peak rotor thrust. However the maneuver pull-up time scale is much slower than the time scale of dynamic stall events occurring locally around the azimuth, i.e., the rotor angular velocity and the blade torsion mode frequency. Thus it is unlikely that benefits from dynamic stall overshoot would be any more manifest in maneuvering flight than in steady state flight. This would seem to be supported by results from RCAS maneuver analyses made with Theodorsen linear unsteady aerodynamics. In fact, these results showed an increase of about 1000 lbs in peak thrust compared to the baseline Leishman-Beddoes result. Similar results were found the analytical investigations by Yeo (Ref. 18).

Blade Airloads

The blade airloads results are presented as section normal force and pitching moment coefficients (times M^2) at four spanwise locations: 67%R, 86.5%R, 92%R and 96.5%R. The R/O2 computations are shown along with measured data over two-revolution intervals during the maneuver. The pitching moment results are presented with the mean values (calculated over the corresponding two-revolution range) removed. This was done to eliminate any skewing of the mean pitching moment values resulting from bad pressure taps near the trailing-edge, that were been discovered in this dataset. (Ref. 3). Results shown for the two-revolution intervals provide a good illustration of the airloads variations during the maneuver as vehicle motions and controls change as a function of time. In general, the airloads evolve gradually from one revolution to the next, but the sensitivity of the airloads, particularly stall related events, may produce significant changes from one rev to the next and this is particularly evident at certain times. The two-revolution results also provides a limited means of assessing the rev-to-rev

variability of experimental measurements, especially for the initial steady-state conditions, and thus helps provide perspective for comparison of calculated and experimental results.

Results for revs 1–2, shown in Fig. 21 generally confirm earlier results for the similar flight counter 8534, marked by high speed compressibility on the advancing blade and little evidence of retreating stall at the $1g$ flight condition. The RCAS results with conventional aerodynamics did not compare as well with data, in part because of the simple uniform inflow wake model used here. This is especially apparent in the airloads near the blade tip. The normal force magnitude and shapes of both normal force and pitching moment curves are good for the R/O2 results.

Figure 22 shows the time-histories for revs 15–16 where the maximum load-factor occurs. Note that RCAS results are not included here in order to make the R/O2 comparisons with data more legible. Three-dimensional transonic effects on the advancing blade, giving high normal force are well captured. The corresponding negative pitching moment peak, however, is not captured as well. Two stall events on the retreating side are seen in the pitching moment data at 86.5%R, however, only the first stall is captured by the R/O2 calculations. Overall, the normal force correlation is much better than the pitching moment correlation.

At revs 19–20, just past peak normal load factor, prediction of airloads faces significant challenges in both advancing blade compressibility effects and retreating blade stall — see Fig. 23. Again, RCAS results are not included to maintain clarity. Triple stall events are particularly evident in pitch moment data at 86.5%R, two retreating blade spikes due to dynamic stall and one spike on advancing blade at low angle of attack but high Mach number. Note the twin retreating blade stall spikes are similar to steady-state high-thrust flight counter 9017 studied by Potsdam *et al.* (Ref. 2). R/O2 results suggest that the CFD model is good at capturing these events but the magnitude and phase of these events needs further improvement via improved grid resolution and turbulence modeling. The advancing blade stall spikes, in both normal force and pitching moment, are very well captured, and portions of the retreating blade stall events for normal force are also captured. Some of the pitch moment stall events are captured, but the twin retreating blade stall events at 86.5%R are not captured as well.

The twin retreating blade stall events at 86.5%R are also seen through revs 23–24 shown in Fig. 24. In this case, surprisingly, the R/O2 results capture this event very well. A similar stall peak at 92%R is also captured well. RCAS results are included here and they are relatively good considering the severity of the operating conditions. Even some stall events are partially captured, e.g., the retreating blade stall at 67.5%R is evident as a sharp drop in normal force and a pitching moment spike. These are both captured by both predictions. A second pitching moment peak thereafter, however, is not captured by RCAS but captured by R/O2. Overall, the RCAS results are not nearly as good as the CFD results, again, because of the nature of the simple lifting-line aerodynamic modeling.

Quasi-Steady Maneuver Analysis

The loose-coupling (LC) approach assumes that the flowfield is periodic in rotor rotational frequency and calculates a steady-state solution. Although this is not strictly valid in a time-varying non-periodic maneuver, it is nevertheless important to explore the feasibility of modeling the maneuver as a series of quasi-steady solutions. The LC approach is very well validated and is certainly faster than the tight-coupling (TC) approach. In this section, we examine revolutions 15–17 of the maneuver, where the highest normal load factor is observed, using a quasi-steady approach.

These LC maneuver calculations were performed in a manner similar to the steady-level trimmed flight calculations, with the controls held fixed. The maneuver inputs were averaged over one rotor revolution, and then each revolution was set-up as an independent steady-state problem with these average inputs; the acceleration terms in the inputs were set to zero. Each solution was run for two-rotor revolutions comprising of eight LC force/deflection exchanges between OVERFLOW-2 and RCAS. The results from these runs were then compared to the time-accurate maneuver calculation presented earlier. Surprisingly, the LC approach was able to capture most of the features present in the time-accurate calculations as shown in Figs. 25 and 34 for airloads and blade loads.

Figure 25 shows the section airloads comparison for the LC and TC calculations for three revolutions. In this case, the data is not shown for clarity. Although three revolutions were calculated as independent problems, they are plotted in sequence to compare with the continuous time-varying TC results. The fact that these three revolutions are solved as independent steady state conditions can be seen by the discontinuities between revolutions. The LC results closely resemble the TC runs, and are also able to capture the pitching moment peaks corresponding to stall events very well.

Grid Effects on Airloads

Since the LC and TC solutions are in close agreements, sensitivity studies may be performed quickly using the LC approach for single revolutions. A grid sensitivity was performed using this approach for the 17^{th} revolution using the fine grid (Ref. 2) with 26.1 million grid points.

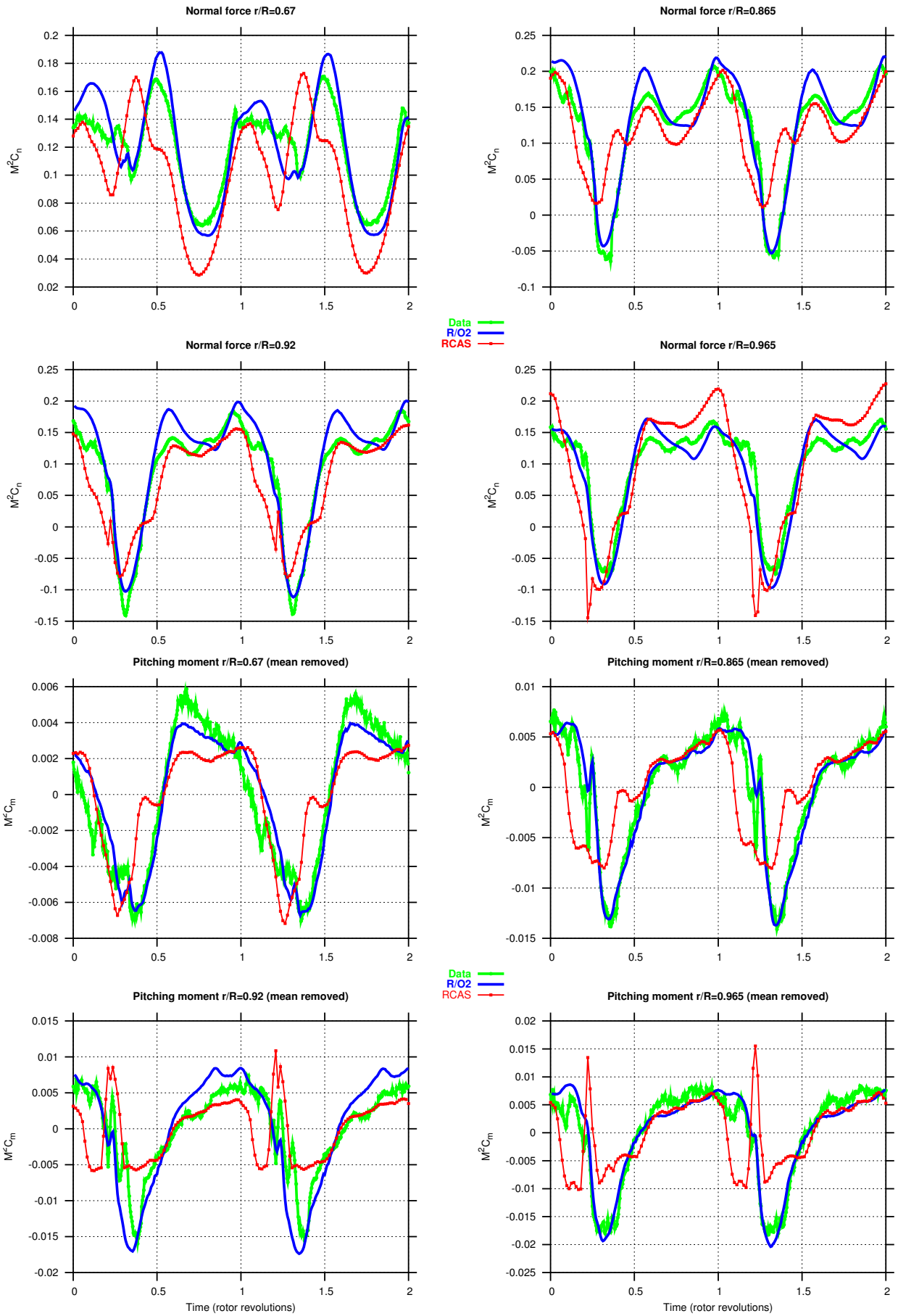

Fig. 21. Section airloads comparison for the initial level flight part of the maneuver (revs 1–2)

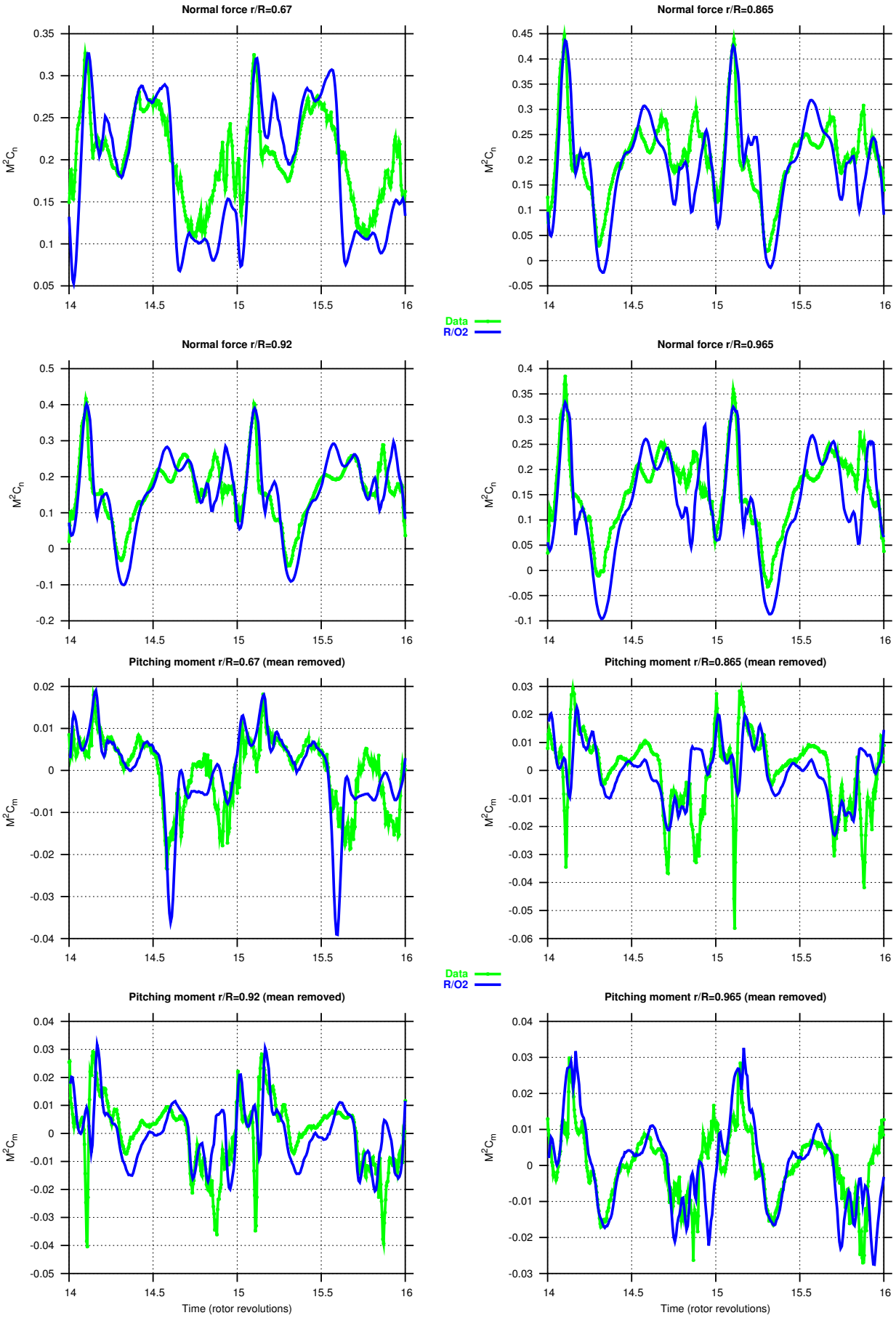

Fig. 22. Section airloads comparison for revs 15–16 of the maneuver

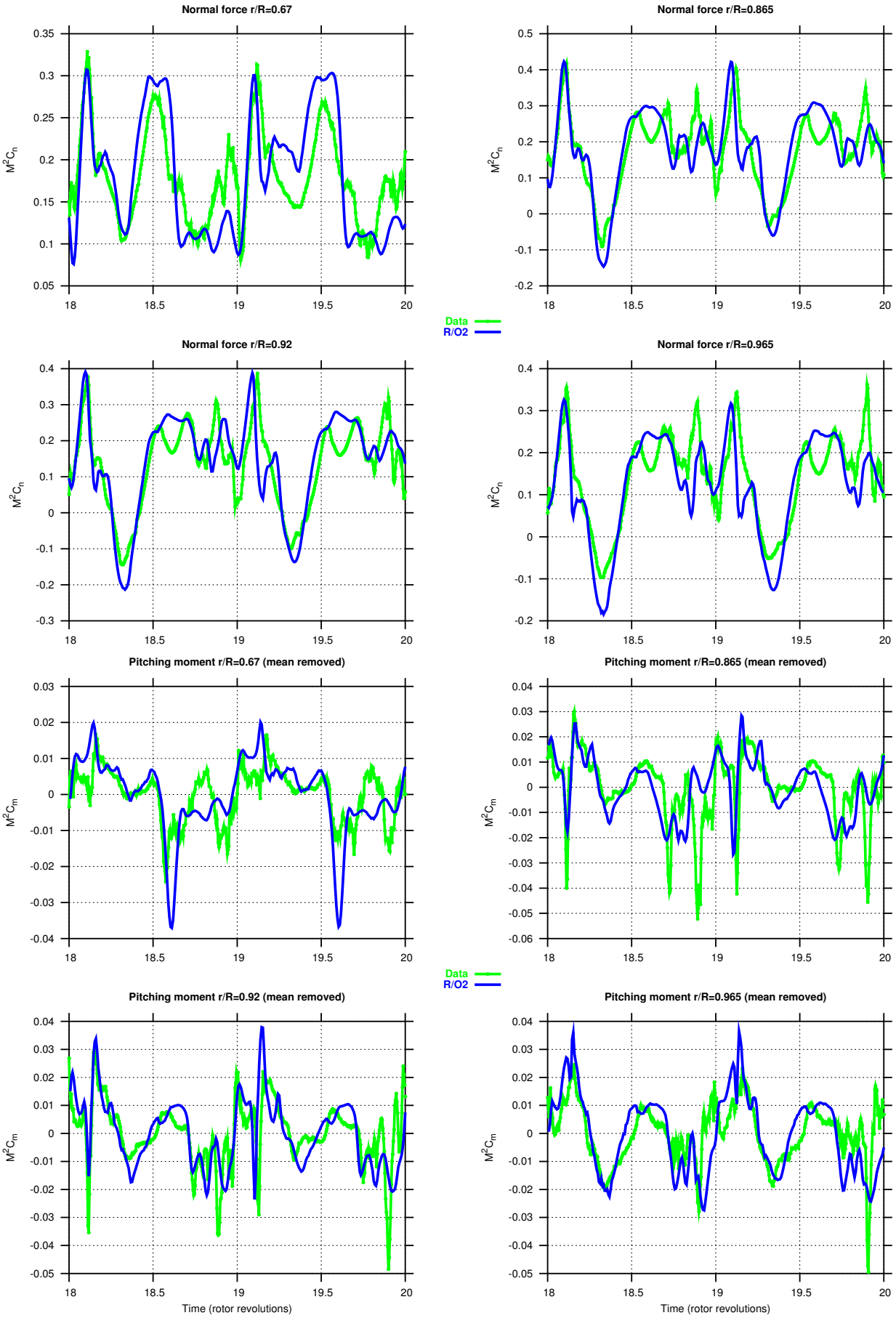

Fig. 23. Section airloads comparison for revs 19–20 of the maneuver

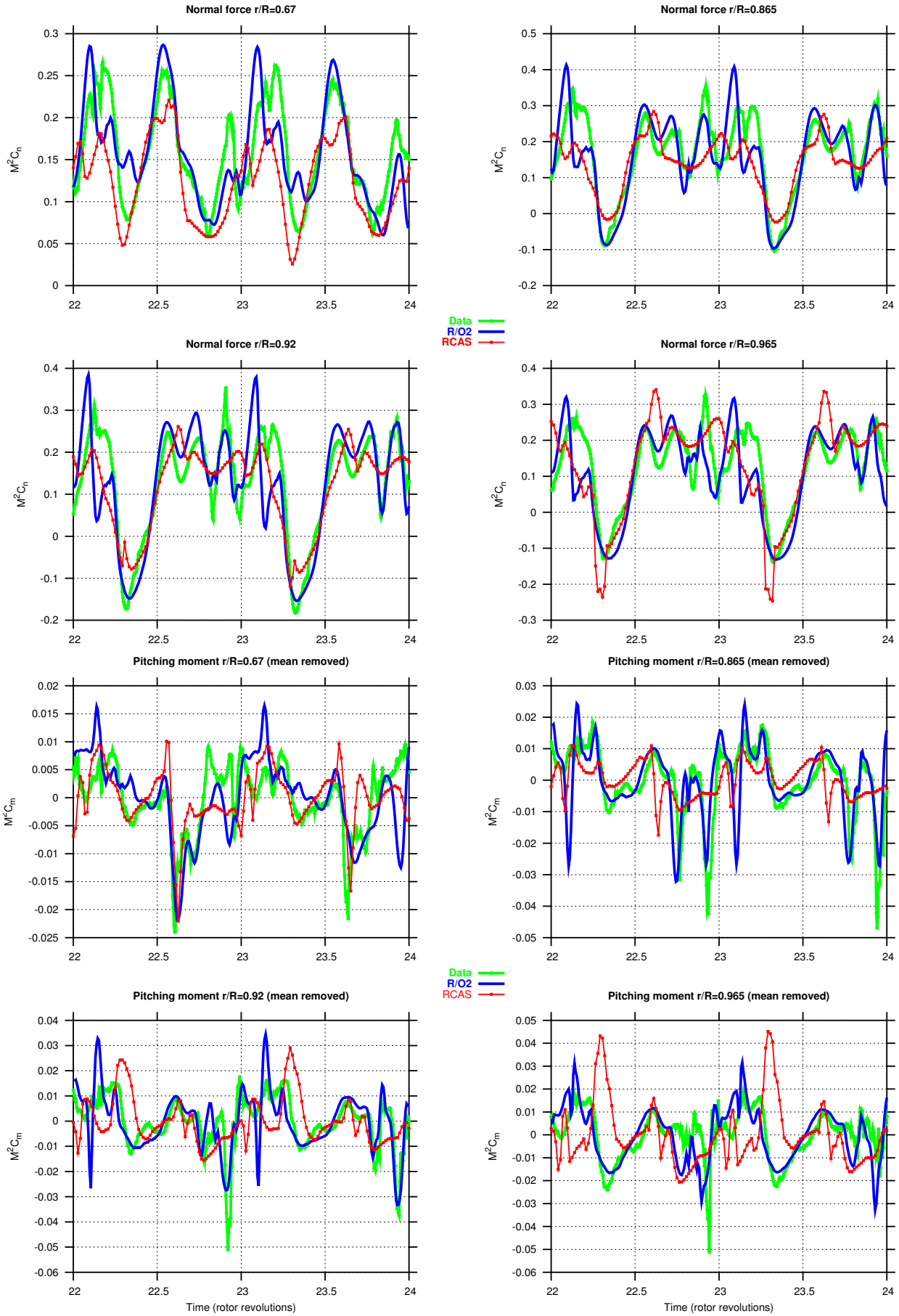

Fig. 24. Section airloads comparison for revs 23–24 of the maneuver

Fig. 25. Section airloads comparison for LC and TC maneuver calculations

This revolution is of special interest because the highest normal load factor occurs here. Some discrepancies in the predicted stall pitching moment peaks observed in Figs. 22–24, may be related to CFD grid resolution. However, in previous calculations using with OVERFLOW-D both the coarse and fine grids were able to capture similar spikes for the flight counter 9017 (Ref. 2). The section airloads are shown in Fig. 26 at four spanwise stations, and compared with the coarse grid solution shown previously. Data is not shown for clarity, although both the results are in good overall agreement with data. The fine grid results show slightly more high-frequency content. However, overall the coarse grid results show most of the dominant features seen in the fine grid results. Stall events occurred slightly earlier with the fine grid than the coarse grid, a result also previously observed in Ref. 2.

Rotor Blade Loads Results

Blade loads are difficult to calculate accurately for demanding flight conditions such as the UTTAS pull-up maneuver. Results for R/O2 and RCAS are compared with the experimental measurements in two ways. First, the per rev 1/2-PTP amplitudes of the calculated results are compared with the measured data for the full maneuver — 24 revs for the R/O2 and 40 revs for RCAS. In addition, blade loads time histories for representative two-rev segments of the full maneuver time history are presented in order to compare the details of the waveforms.

Because of the complexity of blade pitching moments in high speed and high thrust flight conditions, pushrod loads are among the most difficult rotor loads to calculate accurately. Pushrod load calculations for RCAS and R/O2 are shown in Fig. 27 and compared with measured data. It is clear that RCAS alone, using conventional aerodynamics is unable to provide a reasonable result for either the high speed steady-state condition or during the maneuver pull-up. Neither the 1/2-PTP amplitudes nor the waveform shape compare well with the measurements. In particular, the large oscillations in pushrod load and torsion moment (see later) on the retreating side of the disk are not reproduced by the calculations. Results for the R/O2 calculations show significant improvements in the predictions and essentially highlight the need for such coupled CFD/CSD analyses. The 1/2-PTP amplitudes are surprisingly well predicted, but the waveforms also accurately reflect the key features of the measured data, in particular the oscillatory nature of the pushrod loads on the retreating side of the disk. The agreement is especially good for R/O2 during revs 23-24 where the the details of the oscillatory pushrod load is accurately reproduced. In some respects, the differences between the predicted and measured results are no larger than the differences between the measured loads of the individual blades.

Comparisons of calculated and and measured lead-lag damper forces are included for completeness although they cannot be considered a valid test of the accuracy of the R/O2 coupled methodology. Lead-lag dampers are highly nonlinear devices and modeling them is an art in its own right. Use of a linear damper is a very crude approximation. The nonlinear damper model used for the present calculations is also quite simplistic but it gives surprisingly good results, although it does cause a significant increase in computation time. In view of the influence of the lead-lad damper force on blade flatwise and edgewise bending moments, especially near the root of the blade, the nonlinear damper was used for the present results. Results are presented in Fig. 28 and the R/O2 results are better than the baseline RCAS results.

Rotor blade torsion moments are closely related to blade pushrod loads. Torsion moment results for the 30% blade radius are presented in Fig. 29 for RCAS and R/O2 Again, the comparisons are similar to the case of the pushrod loads; RCAS seriously underpredicts the 1/2-PTP amplitude for the high load factor portions of the pull-up and substantially fails to reproduce the details of the waveform. The R/O2 are significantly better although the 1/2-PTP amplitudes are somewhat overpredicted. Similar to the pushrod load waveforms the torsion waveforms capture significant details of the measured waveforms, including the large torsional oscillations associated with blade stall at the higher normal load factors. This is particularly evident for revs 15-16 and 23-24.

Results for rotor blade normal (flatwise) bending moments at 50%R are presented in Fig. 30. The R/O2 1/2-PTP amplitude results are reasonable throughout the maneuver, while RCAS over-predicts the measured blade loads. The R/O2 waveforms are better than the RCAS result, especially the oscillatory loads on the advancing blade.

Results for rotor blade edgewise bending moments at 11.3%R are presented in Fig 31. At this radial location, the edgewise bending moments are largely determined by the lead-lag damper force. Consequently, the results are consistent with the previously discussed damper force results throughout the maneuver; R/O2 1/2-PTP amplitude and waveforms are moderately better than the RCAS results. Over revs 15–20, where the aircraft pulls maximum load-factor, the R/O2 predictions are noticeably better than RCAS. This behavior may be related to the vertical force underprediction by RCAS shown earlier in Fig. 15

Results for rotor blade edgewise bending moments at 50%R are presented in Fig. 32. Here both R/O2 and RCAS 1/2-PTP amplitude results are reasonable throughout the maneuver. The time histories, however, are not as well predicted as other blade loads.

Although experimental data is not available for

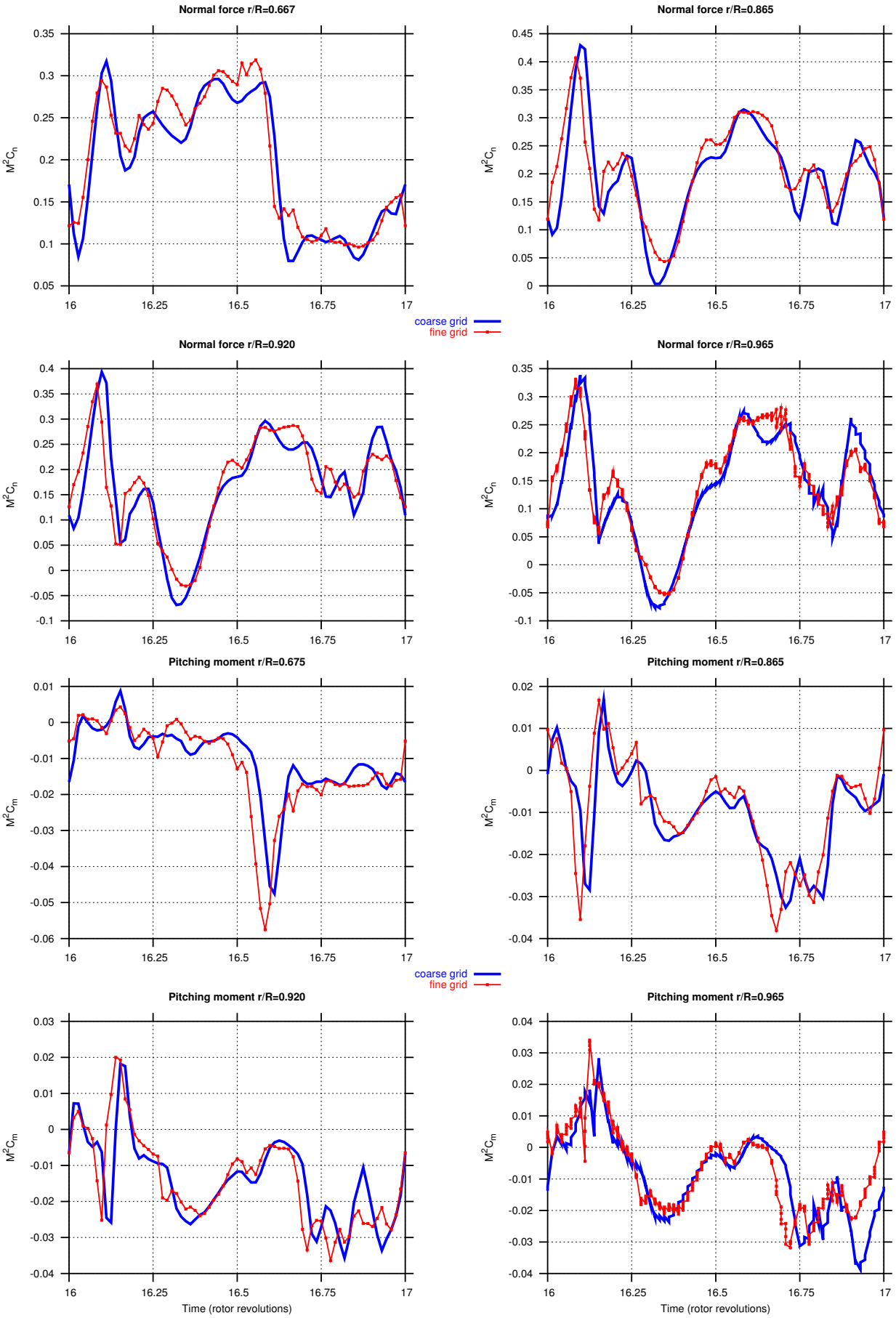

Fig. 26. Section airloads comparison for fine and coarse grids

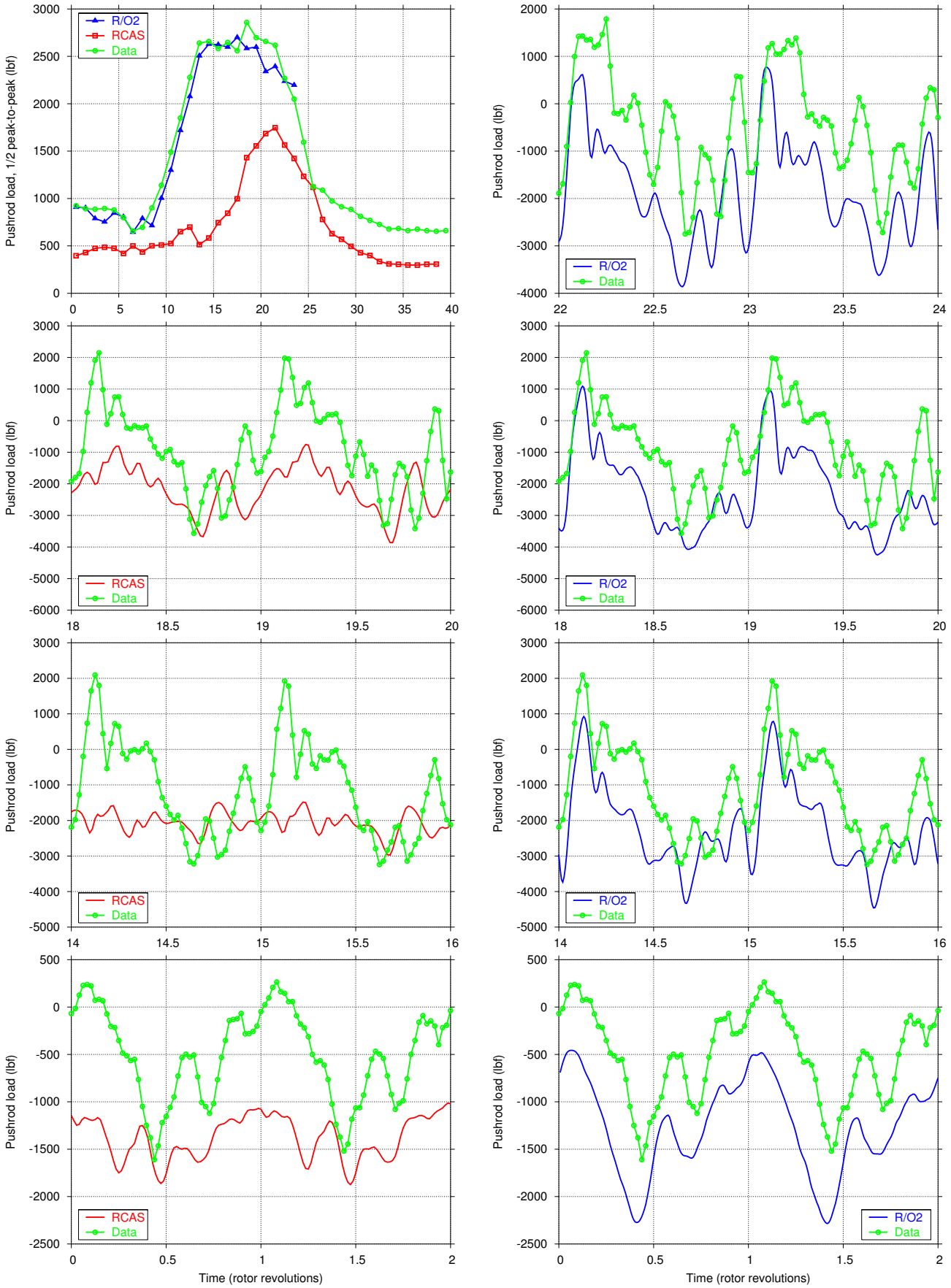

Fig. 27. Pushrod #1 load: 1/2 peak-to-peak and time histories

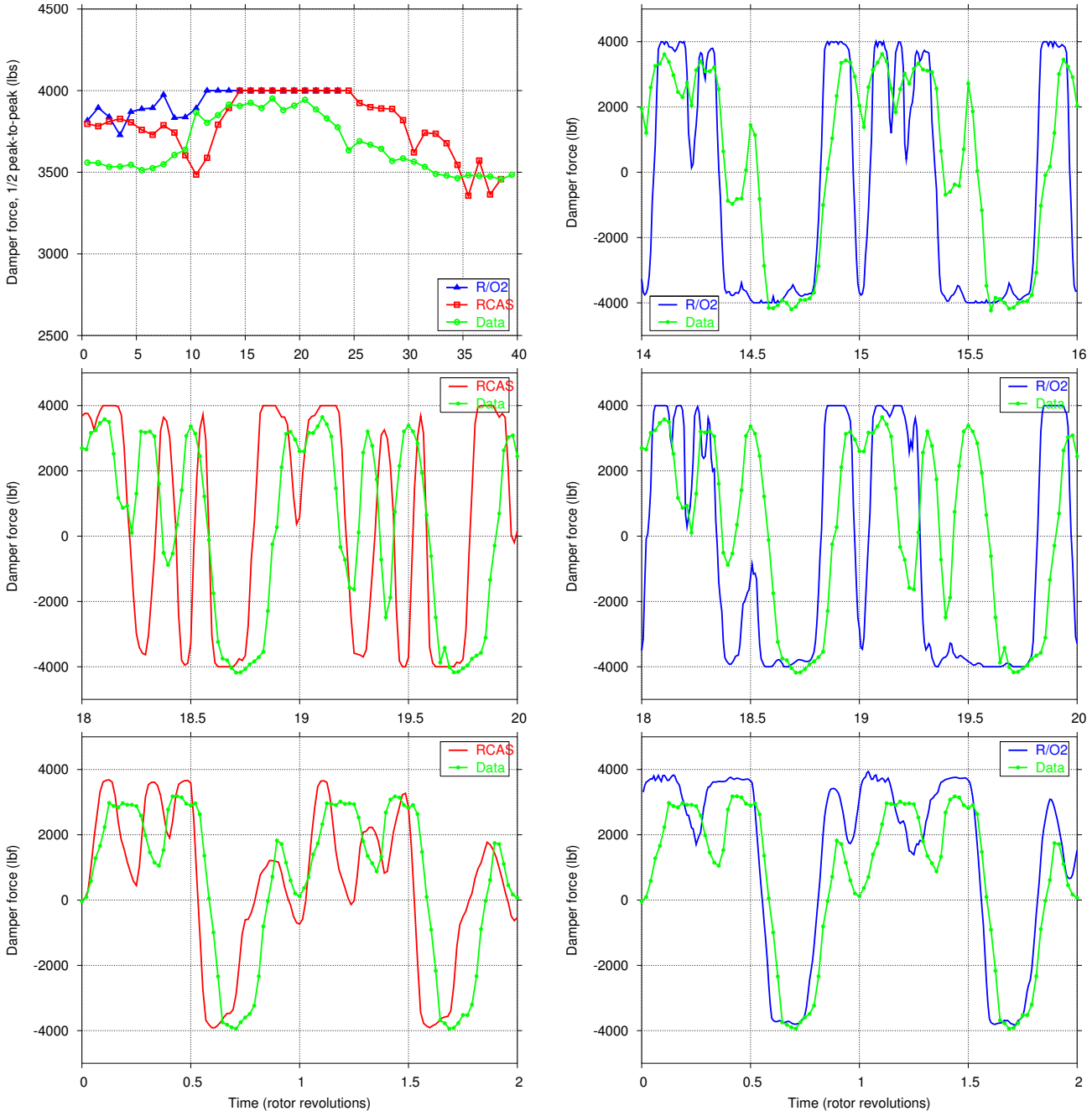

Fig. 28. Lag damper #1 force: 1/2 peak-to-peak and time histories

comparison, the calculated results near the blade tip (93.7%R) for elastic torsional deflections are presented in Fig. 33 to indicate the order of magnitude of aeroelastic deformations that occur in this high speed, high load-factor maneuver. In steady state level flight the 1/2-PTP tip torsion deflections are about 2 deg. and these increase to over 6 deg. during the pull-up. It may be noted that the waveforms are very similar to the torsion moments at 30%R. Corresponding results for RCAS show considerably smaller elastic deflections due to lower blade aerodynamic pitch moments on the advancing blade in both the high-speed level flight and the pull-up portions of the maneuver.

As with the airloads, the structural loads obtained using the LC approach are in good overall agreement with the TC results. An example of this is shown in Figure 34 for the pushrod loads during revs 15–17. The LC results compare equally well with the data as the TC results. This is certainly expected as the airloads prediction using LC was very similar to that using TC as shown previously in Fig. 25. The structural loads prediction using the fine grid, e.g., torsion moment at 30%R shown in Fig. 35, also shows little differences with the coarse grid results.

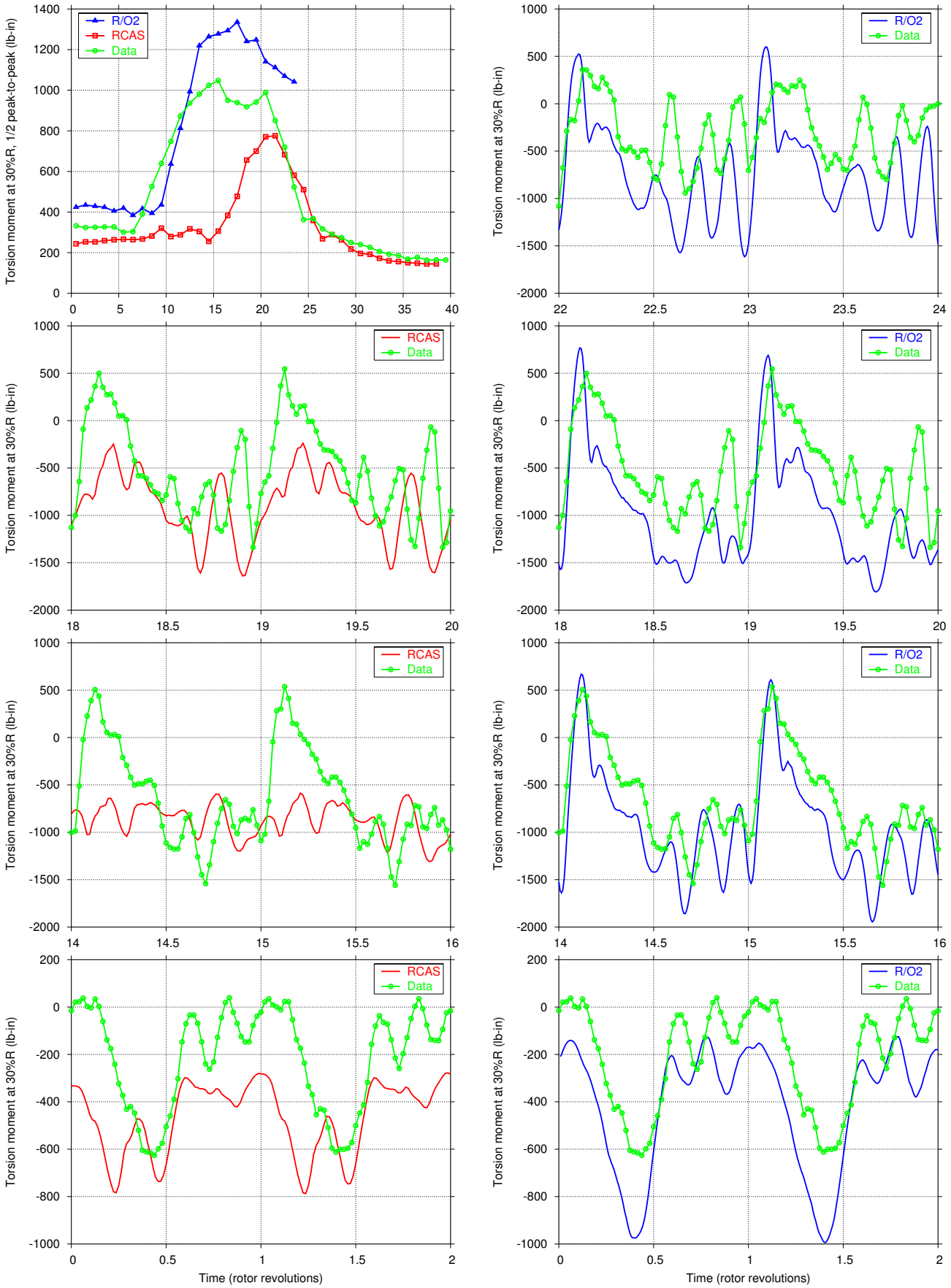

Fig. 29. Torsion moment at 30%R: 1/2 peak-to-peak and time histories

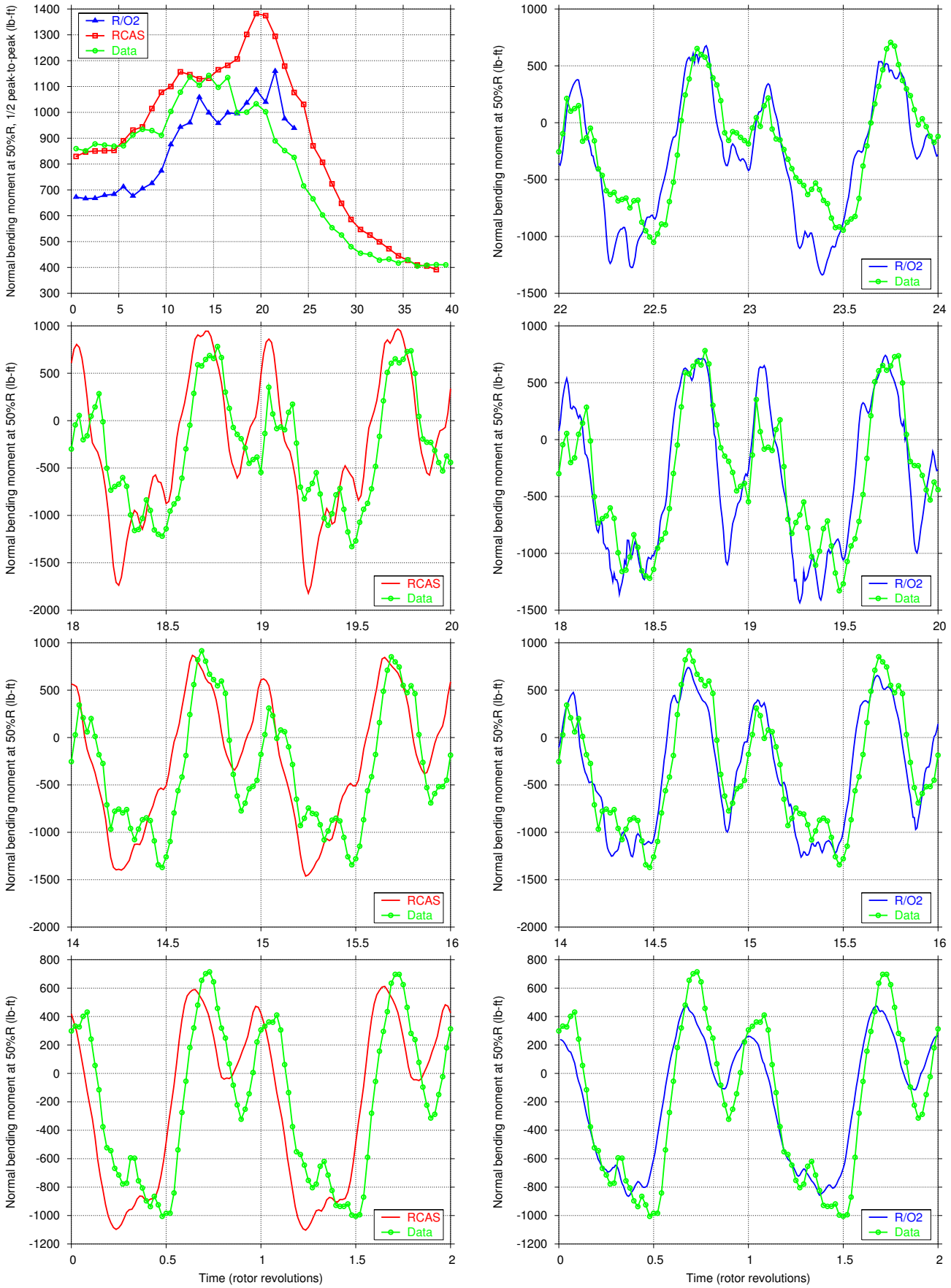

Fig. 30. Normal (flatwise) bending moment at 50%R: 1/2 peak-to-peak and time histories

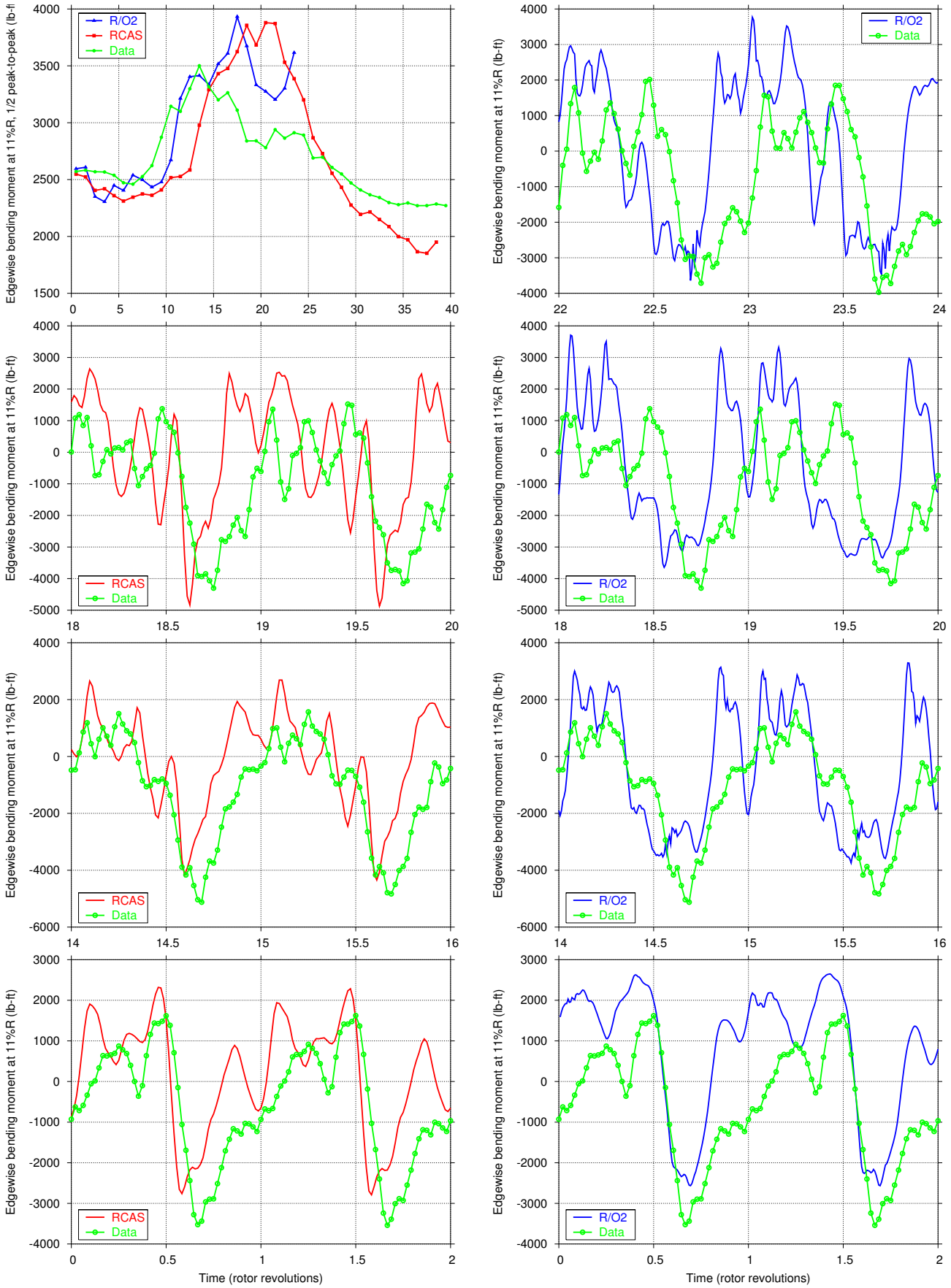

Fig. 31. Edgewise bending moment at 11%R: 1/2 peak-to-peak and time histories

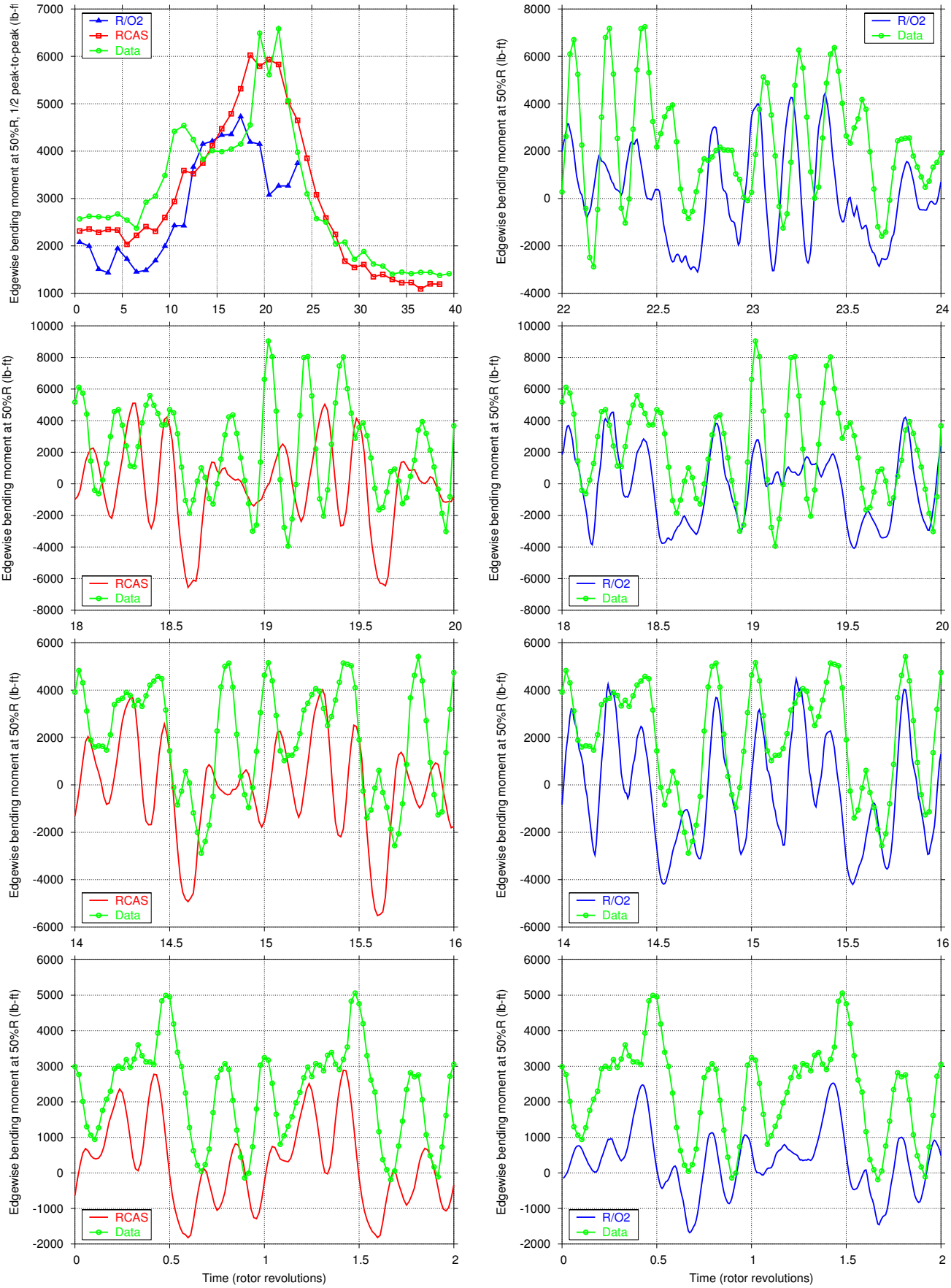

Fig. 32. Edgewise bending moment at 50%R: 1/2 peak-to-peak and time histories

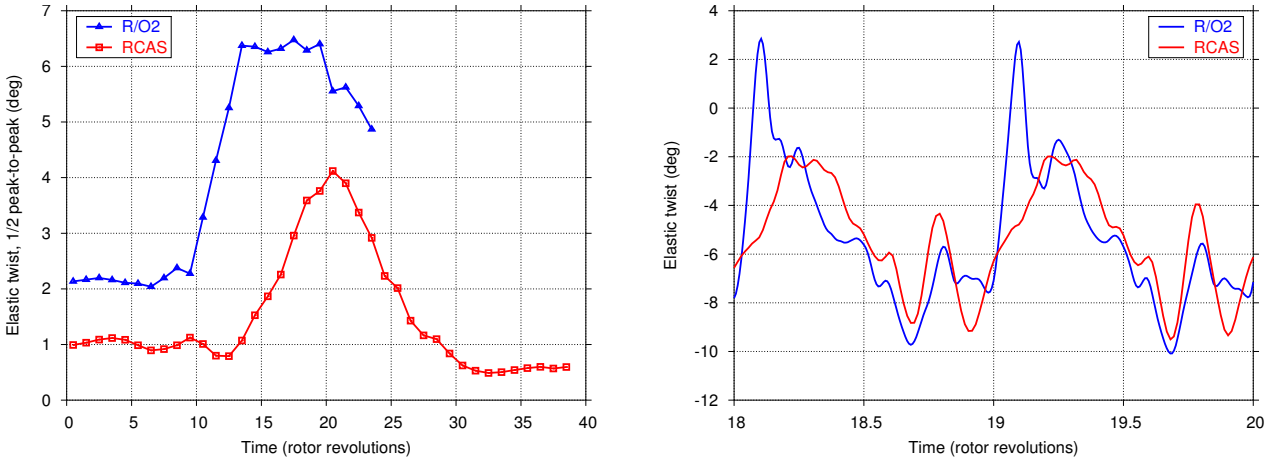

Fig. 33. Blade elastic torsion at 93.7%R (just before swept tip)

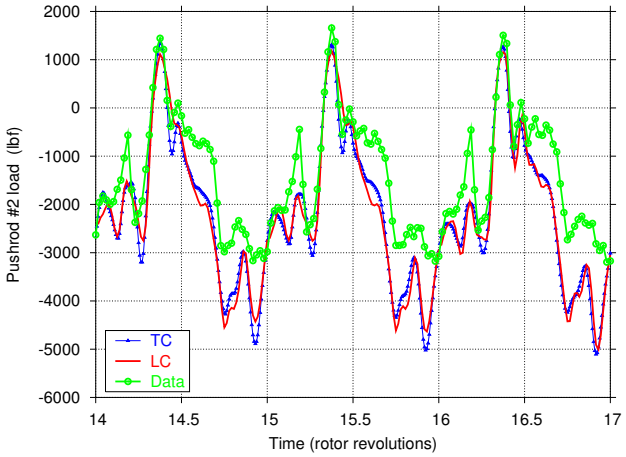

Fig. 34. Pushrod load comparison for LC and TC maneuver calculations

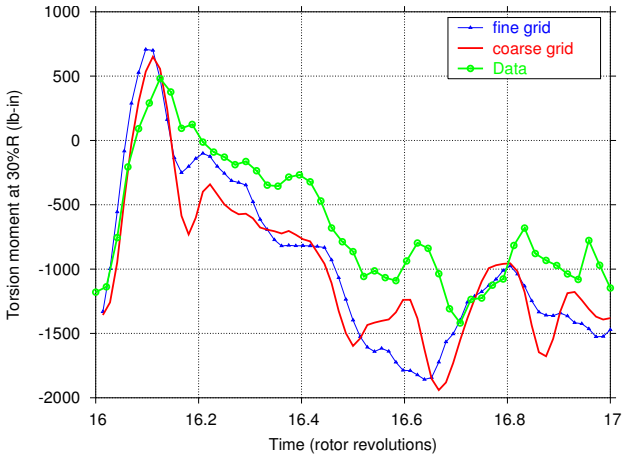

Fig. 35. Torsional moment at 30%R using fine and coarse grids

Pushrod Modeling Sensitivity

Several options for the pushrod and pitch damping modeling were examined while the UH-60A RCAS model was being developed. A stiff pushrod with a linear stiffness of 187792 lbs/ft was used for most of the calculations, while a soft pushrod with a 62631 lbs/ft stiffness was used to examine the sensitivity of load predictions. The smaller pushrod stiffness value was originally accepted as the most reliable value for the UH-60A, but it was only inferred from test and analysis correlations. Uncertainty about it's validity led to direct experimental measurements on the aircraft control system that yielded the larger stiffness value; this has since become generally accepted as the more accurate value. The pitch damper modeling is also uncertain, two parameters are involved, the pitch bearing damping (20 and 100 $\text{ft-lb}/\text{rad}/\text{sec}$) and the pushrod linear damping (240 and 0 $\text{lb}/\text{ft}/\text{sec}$). Typically two combinations of values are used, the 20/240 combination that is the present baseline and the alternative 100/0 combination. The pitch bearing damping of 20 is generally accepted as most accurate; the pushrod damping is generally ignored but Ref. 11 proposed a value of 240 as more reasonable based on analysis of structural loads derived from measured airloads. The effects of pitch damping are examined for the LC maneuver response of rev 17 in Fig. 36 for the baseline stiff pushrod. Here the 20/240 pitch damping combination is superior and this simply reflects the fact that the influence of the pitch bearing damper produces a 1/rev component of pushrod load proportional to 1/rev cyclic pitch angle rotation. Reduction of pitch bearing damping from 100 to 20 reduces the half peak-to-peak pushrod load by nearly 500 lbs with little effect on the dynamic response of the pushrod load waveform.

The sensitivity effect of pushrod stiffness is more complex because it influences torsion dynamics, primarily through the first torsion mode frequency: ≈4.5/rev vs ≈4.0/rev for the stiff and soft pushrods. The effects of pushrod stiffness on the pushrod load are examined in Fig. 37 for the TC maneuver revs 17–20. The pitch damping combination is (100/0). The stiff and soft pushrod loads show moderate differences, presumably reflecting differences in dynamics and aeroelastic response. The soft pushrod is marginally closer to the flight test measurement, but this is misleading since, had the more accurate pitch bearing damping of 20 rather than 100

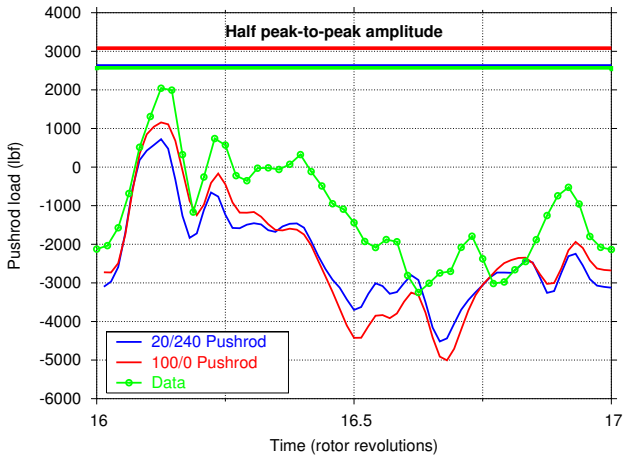

Fig. 36. Effect of pitch-bearing and pushrod damping on pushrod loads

been used, the stiff pushrod would have shown closer agreement with test data.

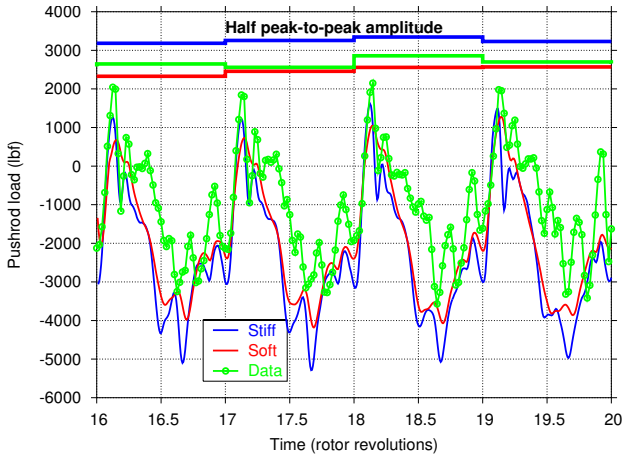

Fig. 37. Effect of soft and stiff pushrod on the pushrod loads

Conclusions

The CFD/CSD tight coupling procedure has been applied to the long-standing and challenging problem of predicting rotor airloads and structural loads in maneuvering flight conditions. Using the RCAS and OVERFLOW-2 codes, the procedure has been shown to work effectively and the computational results give overall very good correlation with flight test data for both airloads and blade structural loads including demanding high load factor conditions.

1. Overall the RCAS/OVERFLOW-2 results yielded substantially better comparisons with flight test data than for conventional aerodynamics methods used in RCAS. A part of the difference may be attributed to the use of simple uniform inflow wake model for RCAS.

2. R/O2 normal force and pitch moment airloads are generally very well predicted in comparison with flight test data, both in $1g$ flight and at high load factors. The normal force airloads are particularly good, capturing multiple blade stall events on the retreating and advancing blade. The pitching moment airloads are in very good agreement in the $1g$ level flight portion of the maneuver, similar to previous results obtained by other investigators for the C8534 test point. At high load factor, the three pitch moment stall events are partially captured, but overall the comparison with test data is less than desired.

3. Quasi-steady results for single revolutions using the associated average maneuver controls and motions for that revolution gave results very close to the full transient maneuver results since the maneuver time scale is slow relative to the time scales of rotor rotation and blade modal frequencies. This finding is of considerable practical significance for CFD/CSD analyses, since this requires only a loose-coupling periodic solution thereby reducing the CPU time requirements to a fraction of that for the full maneuver.

4. R/O2 solution accuracy for the important pushrod control loads and blade torsion moments is very good, both in $1g$ flight and at high load factors. In comparison to flight test data, the 1/2 peak-to-peak and oscillatory waveforms are generally good to excellent. Historically these loads have been most difficult to predict in high speed and maneuvering flight conditions. The torsion and pushrod load oscillatory behavior on the retreating side of the disk at the high load factors exhibits stall flutter oscillations very similar to that observed in the measured data.

5. R/O2 results for the flatwise and chordwise bending moments are generally very good, the latter benefiting substantially from the inclusion of a nonlinear lead-lag damper representation in the structural model.

6. Blade flapping motion is generally good at the start and at the end of the maneuver, but unexplained behavior occurs near the peak normal load factor portion of the maneuver. Flapping magnitude and phase are not well predicted and the R/O2 and RCAS results differ from each other at this point.

7. Overall thrust balance at the peak maneuver load factor of $2.1g$ was determined to be generally consistent with the R/O2 rotor thrust predictions when the contribution of the fuselage and horizontal tail, based on empirical aerodynamics modeling, was included. RCAS rotor peak thrust predictions were roughly 3000 lbs lower than the R/O2 results. The reasons for this deficiency is unknown. The Leishman-Beddoes empirical dynamic stall airloads

method produces a slight reduction in peak thrust compared to linear Theodorsen unsteady aerodynamics.

8. The R/O2 rotor thrust predictions were generally consistent with the derived rotor thrust deduced from integrated measured airloads when an allowance was made for the presumed over-estimation of the measured airloads by approximately 7%.

9. The peak rotor thrust during the maneuver substantially exceeded the McHugh rotor thrust limit for unaccelerated flight. It was deduced that an increase in maximum rotor thrust capability in maneuvering flight results from the pitch-rate-induced gyroscopic roll moment that reduces the retreating blade lift required to maintain roll moment balance relative to that required in unaccelerated flight conditions.

References

[1]Datta, A., Nixon, M. and Chopra, I., "Review of Rotor Loads Prediction With the Emergence of Rotorcraft CFD," 31st European Rotorcraft Forum, Florence, Italy, September 2005.

[2]Potsdam, M., Yeo, H., and Johnson, W., "Rotor Airloads Prediction Using Loose Aerodynamic/Structural Coupling," American Helicopter Society 60th Annual Forum Proceedings, Baltimore, MD, June 2004.

[3]Potsdam, M., Yeo, H., and Johnson, W., "Rotor Airloads Prediction Using Loose Aerodynamic/Structural Coupling," *Journal of Aircraft*, Vol. 43, No. 3, May-June 2006

[4]Sitaraman, J. and Baeder, J., "Evaluation of the Wake Prediction Methodologies Used in CFD Based Rotor Airload Computation," AIAA Paper 2006-3472, 24th AIAA Applied Aerodynamics Conference, San Francisco, CA, June 5-8, 2006

[5]Nygaard, T. A., Saberi, H. A., Ormiston, R. A., Strawn, R. C. and Potsdam, M., "CFD and CSD Coupling Algorithms and Fluid Structure Interface for Rotorcraft Aeromechanics in Steady and Transient Flight Conditions," Presented at the American Helicopter Society 62nd Annual Forum Proceedings, Phoenix, AZ, May 9-11, 2006.

[6]Bousman, W. G. and Kufeld, R. M., "UH-60A Airloads Catalog," NASA TM 2005-212827, August 2005.

[7]Kufeld , R. M. and Bousman, W. G., "High Load Conditions Measured On A UH-60A In Maneuvering Flight," paper presented at the American Helicopter Society 51st Annual Forum Proceedings, Fort Worth, TX, May 9-11, 1995.

[8]Bousman, W. G., "A Qualitative Examination of Dynamic Stall from Flight Test Data," American Helicopter Society 53rd Annual Forum Proceedings, Virginia Beach, VA, April 1997.

[9]McHugh, F. J., "What Are the Lift and Propulsive Force Limits at High Speed for the Conventional Rotor?," American Helicopter Society 34th Annual Forum Proceedings, Washington, DC, May 15–19, 1978.

[10]Saberi, H., Khoshlahjeh, M., Ormiston, R. A., and Rutkowski, M. J., "Overview of RCAS and Application to Advanced Rotorcraft Problems," American Helicopter Society 4th Decennial Specialists Conference on Aeromechanics, San Francisco, CA, January 2004.

[11]Ormiston, R. A., "An Investigation of the Mechanical Airloads Problem for Evaluating Rotor Blade Structural Dynamics Analysis," American Helicopter Society 4th Decennial Specialists Conference on Aeromechanics, San Francisco, CA, January 2004.

[12]Ho, J. C., Yeo, H., and Ormiston, R. A., "Investigation of Rotor Blade Structural Dynamics and Modeling Based on Measured Airloads," American Helicopter Society 63rd Annual Forum Proceedings,

[13]Buning, P., "Consolidation of Time-Accurate, Moving Body Capabilities in OVERFLOW," 6th Overset Composite Grid and Solution Technology Symposium, Ft. Walton Beach, FL, October 2002.

[14]Buning, P., Gomez, R., and Scallion, W., "CFD Approaches for Simulation of Wing-Body Stage Separation," AIAA Paper 2004-4838, 22nd Applied Aerodynamics Conference and Exhibit, Providence, RI, August 2004.

[15]Meakin, R. L., "Automatic Off-Body Grid Generation for Domains of Arbitrary Size," AIAA Paper 2001-2536, 15th AIAA Computational Fluid Dynamics Conference, Anaheim, CA, June 2001.

[16]Tung, C., Caradonna, F. X., and Johnson, W., "The Prediction of Transonic Flows on an Advancing Rotors," *Journal of the American Helicopter Society,* Vol. 31, No. 3, 1986, pp. 4–9.

[17]Farhat, C., Lesoinne, M. and LeTallec, P., "Load and Transfer Algorithms for Fluid/Structure Interaction Problems with Non-Matching Discrete Interfaces: Momentum and Energy Conservation, Optimal Discretization and Application for Aeroelasticity," *Computational Methods in Applied Mechanical Engineering,* Vol. 158, 1998, pp. 95–114.

[18]Yeo, H., "Calculation of Rotor Performance and Loads under Stalled Conditions," American Helicopter Society 59th Annual Forum Proceedings, Phoenix, AZ, May 2003.